

Generalizable Radio-Frequency Radiance Fields for Spatial Spectrum Synthesis

Kang Yang Yuning Chen Wan Du
University of California, Merced

{kyang73, ychen372, wdu3}@ucmerced.edu

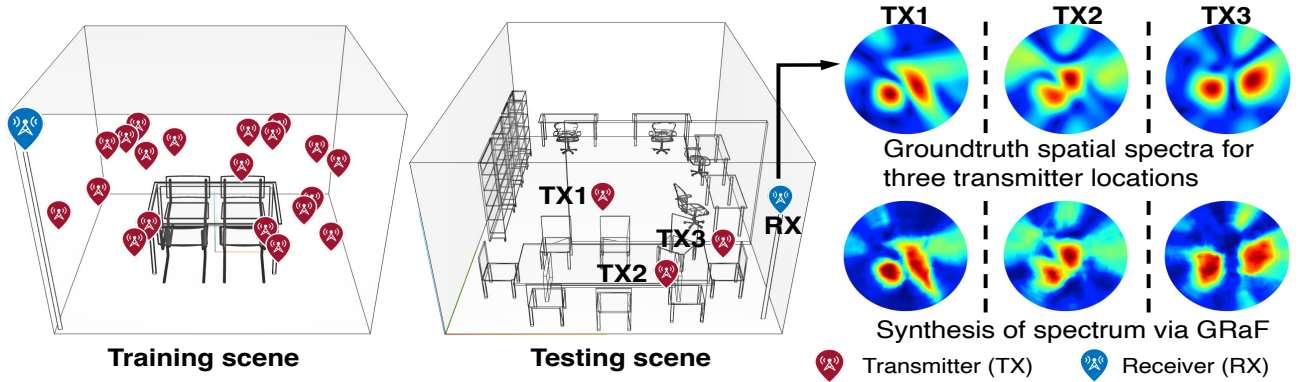


Figure 1. In the training scene, Radio-Frequency (RF) signals from each transmitter are measured across all surrounding directions by the receiver to form a spatial spectrum. Trained on this scene, *GRaF* synthesizes spectra for arbitrary transmitter locations in unseen scenes.

Abstract

We present *GRaF*, *Generalizable Radio-Frequency (RF) Radiance Fields*, a framework that models RF signal propagation to synthesize spatial spectra at arbitrary transmitter or receiver locations, where each spectrum measures signal power across all surrounding directions at the receiver. Unlike state-of-the-art methods that adapt vanilla *Neural Radiance Fields (NeRF)* to the RF domain with scene-specific training, *GRaF* generalizes across scenes to synthesize spectra. To enable this, we prove an interpolation theory in the RF domain: the spatial spectrum from a transmitter can be approximated using spectra from geographically proximate transmitters. Building on this theory, *GRaF* comprises two components: (i) a geometry-aware Transformer encoder that captures spatial correlations from neighboring transmitters to learn a scene-independent latent RF radiance field, and (ii) a neural ray tracing algorithm that estimates spectrum reception at the receiver. Experimental results demonstrate that *GRaF* outperforms existing methods on single-scene benchmarks and achieves state-of-the-art performance on unseen scene layouts.

1. Introduction

The evolution of wireless communication systems, such as WiFi and Sixth Generation (6G) cellular networks, has enabled transformative applications in domains such as smart cities and smart healthcare [15, 26, 47, 49]. These net-

works function as both communication backbones and sensing platforms. Reliable communication requires meticulous network planning to mitigate issues such as dead spots and outages [1], while sensing applications, *e.g.*, WiFi-based localization [3, 43], depend on large volumes of high-quality data to train deep neural networks (DNNs). Traditionally, site surveys [20] are conducted to collect data for communication and sensing. However, conducting these surveys demands dense measurements at numerous locations, which is both time-consuming and labor-intensive [12, 25].

An alternative is to synthesize Radio-Frequency (RF) datasets via propagation modeling, generating spatial spectra that capture the received power from all directions around the receiver (§2.1). Given transmitter and receiver positions, RF propagation modeling estimates the received spectrum while accounting for reflection, diffraction, and scattering [24, 40]. In free space, Maxwell’s equations [35] enable accurate signal computation [55]; however, in complex real-world environments, directly solving them becomes intractable [64]. To approximate these scenarios, ray tracing simulations [14, 17, 19, 34, 61] model propagation paths using Computer-Aided Design (CAD) scene models [30, 38]. However, obtaining accurate CAD models and the high computational cost of ray tracing make such simulations both impractical and unreliable in practice.

Recently, *NeRF²* [65] and *NeWRF* [31] have adapted *Neural Radiance Fields (NeRF)* [28, 33, 37, 45], originally designed for novel view synthesis in the optical domain,

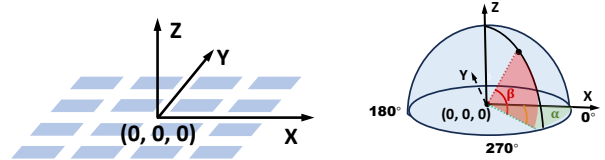
to model RF signal propagation and synthesize spectrum. These methods achieve state-of-the-art performance in RF data synthesis by learning neural radiance fields tailored to RF signals. However, like vanilla NeRF, they tend to overfit the scenes they are trained on, requiring time-intensive retraining for each new scene [29, 37, 51].

This paper introduces *GRaF*, which enhances RF spatial spectrum synthesis within a scene and generalizes to unseen scenes. As illustrated in Figure 1, spectra collected from multiple transmitter locations in a training scene are used to train *GRaF*. After training, *GRaF* can synthesize high-quality spatial spectra for arbitrary locations in new scenes. This capability is supported by our *Interpolation Theorem 1* (§4.1), which establishes that the spectrum at any transmitter location can be approximated by interpolating the spectra of geographically proximate transmitters.

Building on this theory, *GRaF* learns a latent RF radiance field from the spectra of neighboring transmitters, enabling spatial spectrum synthesis beyond the training scene. Constructing such a field requires a fundamentally different approach from optical radiance fields, due to the distinct propagation characteristics of RF signals. Unlike visible light, RF signals have centimeter-scale wavelengths and interact with obstacles through more complex mechanisms, including absorption, reflection, diffraction, and scattering [24, 40]. To account for these interactions, we represent voxel attributes as latent vectors in a learned radiance field, constructed using a geometry-aware Transformer encoder with cross-attention. This encoder processes the spatial spectra of neighboring transmitters along with their geometric relationships to the target transmitter location.

Furthermore, we propose a neural ray tracing algorithm that operates on the latent RF radiance field to estimate the spatial spectrum. This algorithm traces rays outward from the receiver, sampling voxels along each path to account for interactions within the scene. At each voxel, it predicts complex-valued contributions that capture both amplitude and phase variations due to RF propagation. These contributions are then aggregated along each ray, incorporating free-space path loss and phase shifts induced by propagation delay, to compute the received spatial spectrum.

The key contribution of this work is a new paradigm for generalizable RF spatial spectrum synthesis, grounded in an interpolation theory that estimates the spectrum at a target location from the spatial spectra of nearby transmitters. *GRaF* replaces scene-specific NeRF-style approaches with a geometry-aware Transformer that encodes spatial correlations from neighboring transmitters into a latent RF radiance field, followed by a neural ray tracing algorithm that aggregates these features to compute the spatial spectrum. We demonstrate that *GRaF* achieves state-of-the-art performance in both single-scene and cross-scene settings, and further enhances downstream localization performance.



(a) Receiver: 4×4 antenna array (b) Azimuth and elevation
Figure 2. Antenna array; each blue square is an antenna.

2. Preliminary

2.1. Spatial Spectrum

The spatial spectrum characterizes how received RF signal power is distributed across 3D directions (azimuth and elevation) around the receiver when the transmitter emits RF signals. We first present the wireless channel model and then describe how the spatial spectrum is computed.

Wireless Channel Model. A wireless communication system consists of a transmitter and a receiver. The transmitted signal can be represented as a complex number $x = Ae^{j\psi}$, where A is the amplitude and ψ is the phase. As the signal propagates through the wireless channel, its amplitude is attenuated by A_{att} , and its phase is shifted by $\Delta\psi$. The signal received at a single-antenna receiver is given by:

$$y = x \cdot A_{\text{att}}e^{j\Delta\psi} = A \cdot A_{\text{att}}e^{j(\psi+\Delta\psi)}. \quad (1)$$

For a receiver configured as a $M \times N$ antenna array, as illustrated in Figure 2a, the received signal is represented as a matrix $\mathbf{Y} = [y_{m,n}]_{m,n=0}^{M-1,N-1}$, where $y_{m,n}$ denotes the signal received at the (m, n) -th array element. Each element $y_{m,n}$ is computed as follows:

$$y_{m,n} = A \cdot A_{\text{att}}e^{j(\psi+\Delta\psi+\Delta\sigma_{m,n})}, \quad (2)$$

where $A_{\text{att}}e^{j\Delta\psi}$ is the attenuation and phase shift introduced by the channel. The term $\Delta\sigma_{m,n}$ is the geometric phase shift at the (m, n) -th element, caused by its position relative to the array center at $(0, 0, 0)$. It is determined by the element position and the angles of arrival:

$$\Delta\sigma_{m,n} = \frac{2\pi}{\lambda} (md \sin \beta \cos \alpha + nd \sin \beta \sin \alpha), \quad (3)$$

where λ is the signal wavelength, $d = \frac{\lambda}{2}$ is the element spacing, and α and β are the azimuth and elevation angles of the incoming signal, respectively, as shown in Figure 2b.

Spatial Spectrum Computation. It is computed from the received signal matrix \mathbf{Y} to estimate the power distribution over azimuth α and elevation β angles. For a given direction (α, β) , the received signal power is given by:

$$\text{SS}(\alpha, \beta) = \left| \sum_{m=0}^{M-1} \sum_{n=0}^{N-1} y_{m,n} e^{-j\Delta\sigma_{m,n}} \right|^2, \quad (4)$$

where $\Delta\sigma_{m,n}$ is the theoretical geometric phase shift defined in Equation (3). With one-degree resolution and

only the upper hemisphere considered, the spatial spectrum \mathbf{SS} is represented as a matrix of size (N_a, N_e) : $\mathbf{SS} = [SS_{p,q}]_{p=0, q=0}^{N_a-1, N_e-1}$, where $N_a = 360$ (azimuth) and $N_e = 90$ (elevation). Figure 3a shows the 3D spatial spectrum, while Figure 3b depicts the corresponding 2D projection onto the X-Y plane, where the radial distance is $\cos(\beta)$.

2.2. Vanilla NeRF for Spatial Spectrum Synthesis

Vanilla NeRF has recently been adapted for RF spatial spectrum synthesis [31, 65]. It models a 3D scene using a Multi-Layer Perceptron (MLP) with 8-dimensional inputs:

$$\mathcal{F}_\Theta : (\{x, y, z\}, \alpha, \beta, \{x_{tx}, y_{tx}, z_{tx}\}) \rightarrow (\delta, \xi), \quad (5)$$

where $\{x, y, z\}$ are the coordinates of a voxel, and (α, β) denote the azimuth and elevation angles defining the view direction of a ray traced from the receiver. The transmitter coordinates $\{x_{tx}, y_{tx}, z_{tx}\}$ are also included, as each voxel’s properties are influenced by the transmitter’s location. The outputs (δ, ξ) represent the voxel’s RF characteristics, where δ is the attenuation and ξ is the signal emission, with each voxel treated as a secondary RF signal source [5].

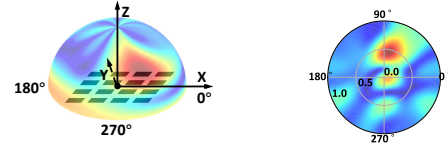
To generate spatial spectrum, *NeRF*² [65] performs ray tracing in each direction of the spectrum. Discrete sample voxels $\{V_1, \dots, V_S\}$ are taken along each ray \mathbf{r} , and the MLP is queried with their coordinates to predict δ and ξ . The result for each ray, $\mathbf{SS}(\mathbf{r})$, is calculated as:

$$\mathbf{SS}(\mathbf{r}) = \sum_{i=1}^S \exp\left(\sum_{j=1}^{i-1} \delta_j\right) \xi_i, \quad (6)$$

where RF signals re-emitted by voxels along the ray are aggregated, with each voxel acting as a source whose contribution is attenuated by intervening voxels.

3. Related Work

Generalization in Optical NeRFs. Optical NeRFs have revolutionized novel view synthesis by learning scene representations from images. However, vanilla NeRF requires extensive per-scene training, limiting its generalization to new scenes [37, 45, 51]. Generalizable NeRFs overcome this limitation by adapting to unseen scenes without re-training [4, 6, 7, 11, 29, 46, 48, 56, 57, 59, 66]. For example, MVSNeRF integrates multi-view stereo with neural rendering to reconstruct radiance fields from a few input views [6], and WaveNeRF employs wavelet-based representations for generalization [56]. GSNeRF incorporates semantics to generate novel views and semantic maps for unseen scenes [11]. These methods cannot be directly applied to RF signals due to fundamental differences in wavelength and propagation behaviors. This work extends generalizable NeRFs to RF domain for spatial spectrum synthesis.



(a) 3D spherical view (b) 2D projection view
Figure 3. Illustration of the spatial spectrum in 3D and 2D views.

RF Spatial Spectrum Synthesis. Several recent works have explored NeRF-style methods in the RF domain [41, 65]. For example, *NeRF*² [65] trains an MLP to compute voxel attributes and uses Equation (6) for ray tracing to compute the spatial spectrum. However, it requires training a separate model for each scene, limiting scalability and hindering generalization to new scenes. NeWRF [31] leverages direction-of-arrival (DoA) priors to reduce ray sampling and improve efficiency, but it requires specialized antenna arrays for DoA measurements, which are often impractical. WiNeRT [41] employs differentiable ray tracing with CAD-based scene geometry, but accurate CAD models are difficult to obtain in practice. RFScape [9] models RF propagation using neural Signed Distance Function (SDF)-based scene geometry, but it requires known object shapes and layouts, limiting practicality. In contrast, *GRaF* requires no scene-specific training, no DoA measurements, and no prior scene models, making it a practical solution for RF spatial spectrum synthesis. GeRaF [32] reconstructs 3D object geometry from near-field RF scans, whereas our work models scene-level RF spectrum synthesis and generalizes across different scenes.

3DGS [22, 60]-based spectrum synthesis methods [27, 53, 58, 62, 63] improve the training and inference times of *NeRF*² [65] within a single scene. In contrast, our work focuses on achieving spatial generalization across scenes.

4. Methodology

Given a set of training scenes $\{1, \dots, K\}$, each containing spatial spectra and transmitter positions $\mathcal{S}^{(k)} = \{(\mathbf{SS}_i^{(k)}, \mathbf{P}_i^{(k)})\}_{i=1}^{N_k}$, where $\mathbf{SS}_i^{(k)} \in \mathbb{R}^{360 \times 90}$ denotes the spatial spectrum and $\mathbf{P}_i^{(k)} \in \mathbb{R}^3$ is the transmitter position, the objective is to learn a model \mathcal{F}_Θ that synthesizes the spectrum $\mathbf{SS}_{\text{target}}^{(j)}$ for a transmitter at position $\mathbf{P}_{\text{target}}^{(j)}$ in any scene j , using its L nearest neighboring transmitters $\mathcal{N}_L^{(j)} \subset \mathcal{S}^{(j)}$. Justification is given in §F.1 of the *Supplementary Materials*. This objective can be formulated as follows:

$$\Theta^* = \arg \max_{\Theta} \prod_{k=1}^K \prod_{i=1}^{N_k} p\left(\mathbf{SS}_i^{(k)} \mid \mathcal{N}_L^{(k)}\left(\mathbf{P}_i^{(k)}\right), \mathbf{P}_i^{(k)}, \Theta\right), \quad (7)$$

where $\mathcal{N}_L^{(k)}\left(\mathbf{P}_i^{(k)}\right)$ denotes the L nearest transmitters to $\mathbf{P}_i^{(k)}$ in $\mathcal{S}^{(k)}$. At inference time, for any scene j (seen

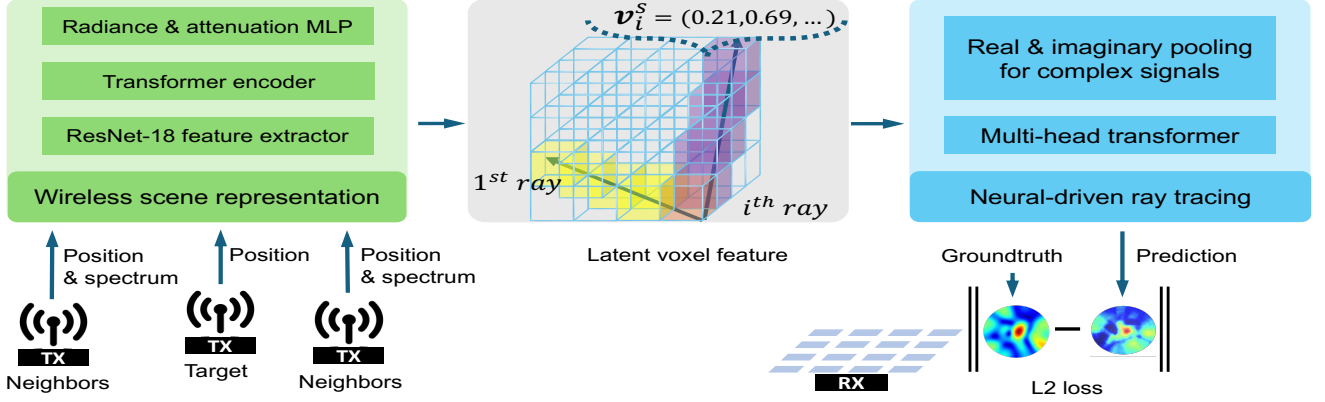


Figure 4. Architecture of *GRaF*. Each voxel is represented by a feature \mathbf{v}_i^s , where i indexes the M rays, and s denotes the voxel’s position along the i -th ray. A neural-driven ray tracing algorithm computes the received signal power for each ray (TX: transmitter, RX: receiver).

or unseen during training), given a target transmitter position $\mathbf{P}_{\text{target}}^{(j)}$ and its neighbors $\mathcal{N}_L^{(j)} \subset \mathcal{S}^{(j)}$, the learned model synthesizes the corresponding spatial spectrum as:

$$\mathbf{SS}_{\text{target}}^{(j)} = \mathcal{F}_{\Theta^*} \left(\mathcal{N}_L^{(j)} \left(\mathbf{P}_{\text{target}}^{(j)} \right), \mathbf{P}_{\text{target}}^{(j)} \right). \quad (8)$$

4.1. RF Spatial Spectrum Interpolation Theory

Theorem 1 (Spectrum Interpolation). *Let $\mathbf{SS}(\mathbf{P})$ denote the spatial spectrum of a transmitter at position $\mathbf{P} \in \mathbb{R}^3$, and let $\mathcal{N}_L(\mathbf{P}) = \{\mathbf{P}_i\}_{i=1}^L$ be its L nearest neighbors with spectra \mathbf{SS}_i . Then the spectrum at \mathbf{P} admits the approximation $\mathbf{SS}(\mathbf{P}) \approx \sum_{i=1}^L w_i \mathbf{SS}_i$, for barycentric weights $\{w_i\}$ determined by the local transmitter geometry. The interpolation error satisfies $\epsilon \leq K \delta^2$, where $\delta = \max_i \|\mathbf{P} - \mathbf{P}_i\|$ denotes the neighborhood radius and K characterizes the environment curvature. The full theorem and proof are provided in §A of the Supplementary Materials.*

4.2. Model Overview

As illustrated in Figure 4, *GRaF* comprises two key components: (i) a latent RF radiance field learned by a geometry-aware Transformer that captures spatial correlations from neighboring transmitters, and (ii) a neural ray tracing algorithm that aggregates latent voxel features along directional rays to compute the spatial spectrum.

Central to this process is a latent variable \mathbf{Z} [36] that encapsulates the scene’s RF propagation characteristics, such as path loss and multipath effects. In particular, \mathbf{Z} represents the interpolation weights from Theorem 1, refined through non-linear transformations to capture propagation behaviors beyond simple linear combinations. Accordingly, the likelihood of the spatial spectrum \mathbf{SS} given the L nearest neighbors \mathcal{N}_L and transmitter position \mathbf{P} is given by:

$$p(\mathbf{SS} | \mathcal{N}_L, \mathbf{P}) = \int p(\mathbf{SS} | \mathbf{Z}, \mathbf{P}) p(\mathbf{Z} | \mathcal{N}_L) d\mathbf{Z}, \quad (9)$$

where $\mathcal{N}_L = \mathcal{N}_L(\mathbf{P})$ denotes the L nearest transmitters to \mathbf{P} . Since \mathbf{Z} encodes global RF propagation properties (e.g.,

materials and geometry), the signal power along each ray depends only on \mathbf{Z} . The neural ray tracing algorithm applies the interpolation theory directionally by deriving ray-specific weights from \mathbf{Z} to estimate the spectrum for each direction. Thus, the likelihood decomposes across rays as:

$$p(\mathbf{SS} | \mathcal{N}_L, \mathbf{P}) = \int \prod_{r=1}^Q p(\mathbf{SS}(r) | \mathbf{Z}, \mathbf{P}) p(\mathbf{Z} | \mathcal{N}_L) d\mathbf{Z}, \quad (10)$$

where $Q = N_a \times N_e$ denotes the total number of rays discretized over azimuth (α) and elevation (β) angles. For example, $Q = 360 \times 90$ at one-degree resolution, covering the upper hemisphere centered at the receiver.

4.3. Latent RF Radiance Field

The latent RF radiance field computes the latent variable \mathbf{Z} , which encodes the scene’s RF propagation characteristics, including path loss, shadowing, and multipath interactions (e.g., reflection and diffraction). This contextual representation enables *GRaF* to generalize spectrum synthesis across diverse scenes by providing a unified encoding of RF propagation behavior. The latent variable \mathbf{Z} is obtained using a parameterized function \mathcal{T}_Ψ that takes as input the L nearest neighbors \mathcal{N}_L and the transmitter position $\mathbf{P} \in \mathbb{R}^3$:

$$\mathbf{Z} = \mathcal{T}_\Psi(\mathcal{N}_L, \mathbf{P}). \quad (11)$$

The architecture of \mathcal{T}_Ψ is designed to effectively integrate both spectral and geometric information from \mathcal{N}_L . It begins with a ResNet-18 feature extractor that processes each neighbor’s spatial spectrum $\mathbf{SS}_i \in \mathcal{N}_L$, producing a compact feature vector that captures high-level patterns such as directional power distribution and signal strength variations. In parallel, the relative positions $(\mathbf{P}_i - \mathbf{P})$ (for each neighbor $\mathbf{P}_i \in \mathcal{N}_L$) are encoded using positional embeddings to preserve the spatial relationships between the target transmitter and its neighbors. These spectral features and geometric embeddings capture both the RF signal characteristics and the geometric context of the scene.

The joint spectral–geometric representations are then processed by a geometry-aware Transformer encoder equipped with cross-attention layers. The cross-attention mechanism dynamically emphasizes the most influential neighboring transmitters by weighting their spectral and geometric features, effectively learning the interpolation weights described in Theorem 1 while capturing non-linear propagation effects such as interference, diffraction, and multipath scattering. The output of the Transformer encoder is subsequently refined by two MLPs, which map the intermediate representation to the final latent variable $\mathbf{Z} \in \mathbb{R}^d$. The resulting \mathbf{Z} serves as a compact contextual encoding that summarizes the scene’s RF propagation behavior and the spatial relationships among neighboring transmitters, enabling *GRaF* to synthesize spatial spectra.

4.4. Neural Ray Tracing Algorithm

The neural ray tracing algorithm synthesizes the spatial spectrum \mathbf{SS}_Θ by leveraging the contextual latent variable \mathbf{Z} . It traces directional rays from the receiver and aggregates latent features along each ray to estimate the signal power in that direction, producing the complete spatial spectrum.

For each ray r with direction (α, β) , we sample S points $\{\mathbf{x}_s\}_{s=1}^S$ along its path, evenly spaced to cover the spatial extent of the scene. At each sampled point \mathbf{x}_s , a voxel-specific feature $\mathbf{v}_s \in \mathbb{R}^d$ is computed by combining the latent variable \mathbf{Z} , the transmitter position $\mathbf{P} \in \mathbb{R}^3$, and positional encodings of \mathbf{x}_s and the ray direction (α, β) :

$$\mathbf{v}_s = \text{MLP}(\mathbf{Z}, \text{PosEnc}(\mathbf{x}_s, (\alpha, \beta), \mathbf{P})), \quad (12)$$

where MLP is a multi-layer perceptron and PosEnc denotes the positional encoding function. The resulting features are then processed by an RF-related function \mathcal{R}_Φ to estimate the signal power for the ray:

$$\hat{\mathbf{S}}\mathbf{S}_\Theta(r) = \mathcal{R}_\Phi(\{\mathbf{v}_s\}_{s=1}^S). \quad (13)$$

To incorporate RF-specific characteristics, \mathcal{R}_Φ models the radiated complex signal and the complex-valued attenuation at each sampled point \mathbf{x}_s along the ray. Inspired by the wireless channel model, the radiated signal $s(\mathbf{x}_s, \alpha, \beta)$ and attenuation $a(\mathbf{x}_s, \alpha, \beta)$ are computed as:

$$\begin{aligned} s(\mathbf{x}_s, \alpha, \beta) &= I_s(\mathbf{x}_s, \alpha, \beta) + j Q_s(\mathbf{x}_s, \alpha, \beta) \\ &= \text{MLP}_s(\mathbf{v}_s), \\ a(\mathbf{x}_s, \alpha, \beta) &= A_s(\mathbf{x}_s, \alpha, \beta) + j B_s(\mathbf{x}_s, \alpha, \beta) \\ &= \text{MLP}_a(\mathbf{v}_s), \end{aligned} \quad (14)$$

where MLP_s and MLP_a map the feature \mathbf{v}_s to the complex signal and complex attenuation, respectively. The attenuation term $a(\mathbf{x}_s, \alpha, \beta)$ encodes both amplitude reduction and phase shift introduced at \mathbf{x}_s . The received ray signal y_r is then obtained by aggregating the contributions from all

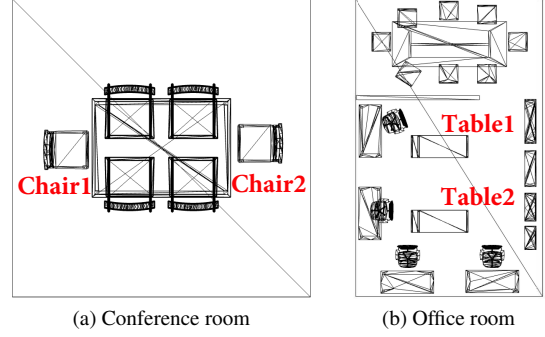


Figure 5. Top-view visualization of two room layouts.

sampled points along the ray. A detailed derivation and proof are provided in §B of the *Supplementary Materials*.

$$y_r = \sum_{s=1}^S \left(\prod_{j=1}^{s-1} a(\mathbf{x}_j, \alpha, \beta) \right) s(\mathbf{x}_s, \alpha, \beta) \cdot \frac{\lambda}{4\pi d_s} e^{-j \frac{2\pi f d_s}{c}}, \quad (15)$$

this aggregation process can be modeled using a Transformer by mapping voxel-wise features (δ, ξ) into token features, where the attention scores naturally represent cumulative attenuation along the ray. Finally, the predicted spatial spectrum value for ray r is obtained as the power of its received signal: $\hat{\mathbf{S}}\mathbf{S}_\Theta(r) = |y_r|^2$.

This procedure is applied to all rays, which discretize the spectrum at one-degree resolution over azimuth and elevation angles, resulting in the complete spatial spectrum \mathbf{SS}_Θ . **Loss Function.** With the spectrum \mathbf{SS}_Θ computed, the overall parameters Θ , which include Ψ (from \mathcal{T}_Ψ) and Φ (from \mathcal{R}_Φ), are optimized to maximize the log-likelihood of the observed spatial spectra, as defined in Equation (7):

$$\begin{aligned} \Theta^* &= \arg \max_{\Theta} \log p(\mathbf{SS}_\Theta | \mathcal{N}_L, \mathbf{P}) \\ &= \arg \max_{\Theta} \log \int \prod_{r=1}^Q p(\mathbf{SS}(r) | \mathbf{Z}, \mathbf{P}) p(\mathbf{Z} | \mathcal{N}_L) d\mathbf{Z}. \end{aligned} \quad (16)$$

Direct computation of this integral is intractable due to the high dimensionality of \mathbf{Z} . Because \mathbf{Z} is deterministically produced by the latent RF radiance field, the optimization reduces to a supervised reconstruction problem. The derivation is provided in §C of the *Supplementary Materials*.

$$\Theta^* = \arg \min_{\Theta} \sum_{r=1}^Q \left\| \mathbf{SS}(r) - \hat{\mathbf{S}}\mathbf{S}_\Theta(r) \right\|^2. \quad (17)$$

5. Experiments

Implementation details are provided in §D of the *Supplementary Materials*. We first evaluate *GRaF* in a single-scene setting, and then assess its cross-scene performance.

5.1. Experimental Setup

• **Datasets** (1) RFID DATASET: Introduced by *NeRF²* [65], RF Identification (RFID) operates in 915 MHz, with a re-

Table 1. Model performance for the single-scene settings.

Models	MSE↓	LPIPS↓	PSNR↑	SSIM↑
KNN	0.089	0.357	15.16	0.543
KNN-DL	0.048	0.198	20.81	0.675
<i>NeRF</i> ²	0.052	0.274	19.93	0.704
<i>GRaF</i>	0.038	0.136	21.94	0.766

ceiver positioned at a fixed location and equipped with a 4×4 antenna array. The dataset consists of 6,123 transmitter locations, each associated with a spectrum.

(II) **MATLAB DATASET:** We consider two representative indoor layouts: a conference room and an office room. Their geometries are illustrated in Figure 5, with dimensions of $9.8 \text{ ft} \times 9.8 \text{ ft} \times 8.2 \text{ ft}$ and $26.2 \text{ ft} \times 16.4 \text{ ft} \times 9.8 \text{ ft}$, respectively. Each layout is represented by a CAD model and further diversified into multiple scene versions by modifying object placements using Blender. For the conference room layout (Figure 5a), we define three scene versions: *ConferenceV1* includes both Chairs 1 and 2, *ConferenceV2* includes only Chair 1, and *ConferenceV3* includes neither Chair 1 nor Chair 2. For the office room layout (Figure 5b), we similarly define three scene versions: *OfficeV1* includes both Tables 1 and 2, *OfficeV2* includes only Table 1, and *OfficeV3* includes neither Table 1 nor Table 2.

In each scene version, a receiver with a fixed antenna array is positioned, and transmitters are randomly distributed throughout the space. A total of 4,416, 4,453, 3,107, 8,481, 7,274, and 4,894 transmitters are placed to collect spatial spectra for each scene version using MATLAB ray tracing simulation [34]. Unless stated otherwise, 80% of the data is for training and 20% for testing.

(III) Additional layouts, *i.e.*, a bedroom and an outdoor scene, are described in §E of the *Supplementary Materials*.

• **Baselines** We compare *GRaF* against three baselines.

(I) **K-NEAREST NEIGHBORS (KNN):** It predicts the spatial spectrum at a target transmitter location by averaging the spectra of the L nearest neighbors, ensuring L matches *GRaF* for a fair comparison.

(II) **KNN-DL:** Similar to KNN, this approach assigns a weight matrix of dimension (N_a, N_e) to each neighbor instead of using equal averaging. Each pixel of the spectrum is given a learnable weight, and the target spectrum is obtained by a weighted summation of all neighbors’ spectra using their corresponding weight matrices. The weight matrices are optimized using an ℓ_2 loss. Further details are provided in §A.2 of the *Supplementary Materials*.

(III) ***NeRF*²:** It is introduced in §2.2. *NeWRF* [31] is essentially the same as *NeRF*², but additionally uses DoA measurements to reduce the number of rays. Since DoA data is difficult to obtain in practice, we treat *NeRF*² and *NeWRF* as equivalent methods in our evaluation. Other methods, *e.g.*, *WiNeRT* [41] and *RFScape* [9], are not di-

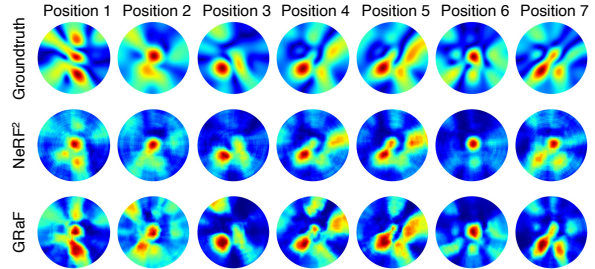


Figure 6. Visual comparison of synthesized spatial spectra.

rectly comparable since they require prior scene models.

• **Metrics** Mean Squared Error (MSE) measures the average squared difference between the predicted and ground-truth signal power across all directions in the spatial spectrum, serving as the domain loss. Since the spatial spectrum (see Figure 3b) can be visualized as an image, image quality metrics are used to assess pixel-level differences and structural consistency [52], capturing directional patterns. Accordingly, we evaluate performance using four widely adopted metrics: MSE↓, Learned Perceptual Image Patch Similarity (LPIPS↓), Peak Signal-to-Noise Ratio (PSNR↑), and Structural Similarity Index Measure (SSIM↑).

5.2. Single-Scene Performance

There are seven scenes in total: one from the RFID dataset and six from the MATLAB dataset (*ConferenceV1–V3*, *OfficeV1–V3*). In this section, we train and evaluate a separate model for each scene, using 80% of the data for training and the remaining 20% for testing.

Analysis. We first present the spatial spectra of four randomly selected transmitter locations, alongside the spectra synthesized by *NeRF*² and *GRaF*, as illustrated in Figure 6. Visually, the spectra synthesized by *GRaF* closely match the ground truth, outperforming those generated by *NeRF*². Consistent with this visual comparison, *GRaF* achieves superior metric scores, as illustrated in Table 1. Compared to the KNN and KNN-DL, *GRaF* improves PSNR by 44.7% and 5.5%, respectively. These results demonstrate that neighboring spatial spectra are indeed helpful for predicting the target transmitter’s spectrum. However, KNN’s simple averaging approach fails to capture the intricate spatial relationships among the neighboring spectra. KNN-DL further improves upon KNN’s performance, indicating that a careful interpretation of neighboring spectra can enhance the prediction accuracy. Nevertheless, KNN-DL does not account for the geometric relationships among spectra, limiting its effectiveness. Finally, *GRaF* outperforms *NeRF*² by 26.9%, 50.4%, 10.2%, and 8.8% in terms of MSE, LPIPS, PSNR, and SSIM, respectively. This improvement highlights *GRaF*’s ability to leverage neighboring spatial spectra to learn latent voxel features that capture complex propagation behaviors and dynamically assign weights using an attention mechanism during ray tracing.

Table 2. Model performance on the unseen scenes settings.

Models	MSE↓	LPIPS↓	PSNR↑	SSIM↑
KNN	0.083	0.361	14.77	0.552
KNN-DL	0.053	0.279	19.04	0.614
<i>NeRF</i> ²	0.065	0.337	17.36	0.691
<i>GRaF</i>	0.039	0.215	20.96	0.705

5.3. Generalization to Unseen Scenes

We evaluate the generalization capability of *GRaF* across unseen scenes, particularly when object configurations within the layout are changed. Specifically, we train two models separately for the conference room and office room layouts. For the conference room, the model is trained on ConferenceV1 and tested on the test splits of ConferenceV2 and ConferenceV3. For the office room, the model is trained on OfficeV1 and tested on OfficeV2 and OfficeV3. All baseline methods are trained and evaluated under the same settings for fair comparison. The inverse setting, *i.e.*, the training and testing scenes are swapped, is provided in §E.2 of the *Supplementary Materials*.

Analysis. Table 2 presents the average quantitative results for the two layout models. Compared to the single-scene setting (Table 1), KNN achieves similar performance in both scenarios, highlighting that neighboring spatial information consistently provides value. In contrast, the performance of KNN-DL and *NeRF*² declines in the unseen scene setting due to their reliance on models overfitted to the training scenes, which limits their generalization capabilities. However, because the differences between the training and testing scenes involve only minor modifications, such as adding or removing one or two tables or chairs, the performance degradation is moderate, with PSNR drops of 8.51% for KNN-DL and 12.90% for *NeRF*². By comparison, *GRaF* achieves the highest accuracy in both settings by leveraging geometry-aware latent RF radiance fields and a neural ray tracing algorithm, enabling effective generalization across diverse scene layouts.

5.4. Generalization to Unseen Layouts

We further evaluate the generalization capability of *GRaF* under a more challenging setting. Specifically, a model is trained on all three versions of the conference layout, *i.e.*, the training splits of ConferenceV1–V3, and tested on all three versions of the office layout, *i.e.*, OfficeV1–V3. The reverse experiment is also conducted, where the model is trained on OfficeV1–V3 and tested on ConferenceV1–V3. For fair comparison, the three baseline methods are evaluated under the same experimental settings.

Analysis. Table 3 presents the quantitative results for unseen layouts. KNN demonstrates consistent performance across settings with slight PSNR fluctuations, reflecting the effectiveness of neighboring spatial spectrum information.

Table 3. Model performance on the unseen layouts settings

Models	MSE↓	LPIPS↓	PSNR↑	SSIM↑
KNN	0.085	0.359	15.32	0.539
KNN-DL	0.087	0.429	14.94	0.498
<i>NeRF</i> ²	0.092	0.477	12.76	0.481
<i>GRaF</i>	0.042	0.268	17.81	0.629

Table 4. Ablated versions of *GRaF* in unseen scene settings.

Model variations	LPIPS↓	PSNR↑
Without cross-attention layer	0.239	19.37
Without neural ray tracing	0.379	16.79
Full model (<i>GRaF</i>)	0.215	20.96

In contrast, KNN-DL and *NeRF*² show significant performance declines in unseen layouts compared to single-scene settings. KNN-DL’s PSNR drops by 28.2% and *NeRF*²’s by 35.9%, highlighting their limited generalization due to scene-specific training. *GRaF* achieves the highest accuracy across all settings, demonstrating robust generalization. This is attributed to its geometry-aware voxel features and neural ray tracing, which enable it to adapt to diverse scenes. However, the spectra synthesized by *GRaF* in cross-layout experiments are of lower quality than those in single-scene experiments. This performance decline is due to challenges posed by varied layouts and object materials [55].

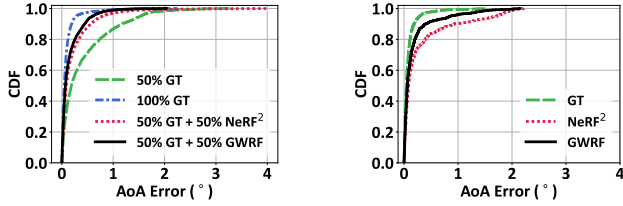
The trained *GRaF* is also evaluated on additional layouts (Bedroom and Outdoor) as well as a real-world dataset, introducing diverse spatial characteristics. The Bedroom features confined spaces with rich multipath propagation; the Outdoor represents a large-scale open environment with sparse reflectors; and the RFID dataset introduces real-world noise, hardware variability, and temporal effects. Results are provided in §E.3 of the *Supplementary Materials*.

5.5. Ablation Study

This section follows the unseen-scene setting described in §5.3, with results shown in Table 4. The impact of neighbor number L is given in §E.4 of the *Supplementary Materials*.

Latent RF Radiance Field. In the parameterized function \mathcal{T}_ψ of our model, we adopt a geometry-aware cross-attention layer to learn contextual latent representations. To evaluate the effect of attention mechanisms, we replace the cross-attention layer with a simpler dot-product attention layer. A comparison between the first and third rows in Table 4 shows that *GRaF* achieves slightly better performance with the cross-attention mechanism. This result suggests that *GRaF*’s generalization ability stems from its capacity to model interactions across neighboring spatial spectra.

Neural Ray Tracing. We replace our neural ray tracing algorithm with a simplified method based on Equation (6), which models each voxel using only two attributes: signal emission and attenuation. A comparison between the



(a) For AANN training

(b) For AANN testing

Figure 7. Spectrum-based AoA estimation via AANN [2].

second and third rows in Table 4 shows that our neural approach outperforms the simplified method, highlighting the advantages of voxel-level vector representations and the model’s ability to learn adaptive fusion weights. The difference between the ablated version of *GRaF* (“without neural ray tracing” in Table 4) and *NeRF*² lies in scene representation. While the ablated *GRaF* retains the parameterized function \mathcal{T}_Ψ for processing neighboring spectra, it simplifies voxel modeling and uses the ray tracing module from *NeRF*². As shown in Table 2, *NeRF*² achieves a PSNR of 17.36 dB, while the ablated version of *GRaF* yields 16.79 dB (Table 4). This performance gap underscores the importance of *GRaF*’s full pipeline.

5.6. Impact of RF Frequency Bands

To examine the impact of frequency bands, we collect three datasets in a conference room (Figure 5a) at 928 MHz, 2.412 GHz, and 5.805 GHz. *GRaF* is trained on each dataset. As shown in Table 5, *GRaF* adapts well to different bands while maintaining high-quality synthesized spectra. This design is justified since each band supports different wireless technologies (e.g., 5G, WiFi), requiring dedicated hardware for signal reception and processing [13, 44, 54].

Additionally, in Table 6, we evaluate a version of *GRaF* trained only on the 2.412 GHz dataset (voxel size $\lambda \approx 0.124$ m) and directly tested on the 928 MHz and 5.805 GHz datasets without retraining. During testing, the voxel size is held fixed at 0.124 m. This cross-frequency evaluation reveals a noticeable performance drop, primarily due to two factors. First, RF propagation characteristics vary with frequency. At 928 MHz, signals experience stronger penetration and reduced attenuation, while at 5.805 GHz, they are more prone to scattering and absorption. These variations in wave behavior limit the model’s ability to generalize across bands. Second, maintaining a fixed voxel size leads to spatial resolution mismatch. For 928 MHz ($\lambda \approx 0.323$ m), the voxel grid is unnecessarily fine, preserving details but increasing computational cost. In contrast, for 5.805 GHz ($\lambda \approx 0.052$ m), the voxel size is too coarse to resolve fine-scale propagation effects.

5.7. Case Study: Angle of Arrival (AoA) Estimation

The synthesized spatial spectrum can be used for downstream tasks such as Angle of Arrival (AoA) estimation for

Table 5. Training separately on each frequency band.

	928 MHz	2.412 GHz	5.805 GHz
PSNR \uparrow	25.70	24.53	24.91

Table 6. Training only on the 2.412 GHz frequency band.

	MSE \downarrow	LPIPS \downarrow	PSNR \uparrow	SSIM \uparrow
928 MHz	0.104	0.362	14.84	0.576
5.805 GHz	0.218	0.467	11.61	0.493

wireless localization [2]. We use an angular artificial neural network (AANN), which consists of a ResNet-50 backbone followed by an MLP head, to process the spectrum and estimate the AoA. This estimated AoA corresponds to the line-of-sight (LoS) propagation direction between the transmitter and receiver, enabling transmitter localization.

By generating synthetic training datasets, *GRaF* significantly reduces the data collection effort required to train the AANN. To demonstrate the benefits of the high-quality spectra synthesized by *GRaF*, we evaluate using the following two strategies for the training and testing stages:

(i) Synthesized Spectra for AANN Training. An AANN is trained on four datasets: (1) 50% ground truth (GT), (2) 50% GT combined with 50% *NeRF*²-synthesized spectra, (3) 50% GT combined with 50% *GRaF*-synthesized spectra, and (4) 100% GT. All training datasets use the same transmitter locations, and each trained AANN is evaluated on a shared testing set with consistent transmitter positions. Figure 7a presents the cumulative distribution function (CDF) of the estimated AoA error. The *GRaF*-augmented dataset reduces the estimation error by 61.6% compared to training on 50% GT alone, and by 25.8% relative to the *NeRF*²-augmented dataset. These results demonstrate that *GRaF* produces high-quality spectra that effectively improve localization model training.

(ii) Synthesized Spectra for AANN Testing. An AANN is trained on GT spectra and evaluated on three types of test datasets: GT, *NeRF*²-synthesized spectra, and *GRaF*-synthesized spectra. All test spectra correspond to the same transmitter locations. Figure 7b demonstrates that *GRaF*’s spectra yield more accurate AoA estimations, highlighting the superior fidelity of *GRaF*’s synthesized spectra.

6. Conclusion

This paper presents *GRaF*, a generalizable RF radiance field framework for spatial spectrum synthesis. We first establish the interpolation theory in the RF domain as the theoretical foundation. *GRaF* integrates a geometry-aware latent RF radiance field to capture spatially correlated propagation characteristics and employs a neural ray tracing algorithm to aggregate these features for accurate spectrum computation. Experimental results show that *GRaF* generalizes across scenes and enhances downstream task performance.

References

- [1] Md Maruf Ahamed and Saleh Faruque. 5G network coverage planning and analysis of the deployment challenges. *Sensors*, 21(19):6608, 2021. 1
- [2] Zhenlin An, Qiongzheng Lin, Ping Li, and Lei Yang. General-Purpose Deep Tracking Platform across Protocols for the Internet of Things. In *ACM International Conference on Mobile Systems, Applications, and Services (MobiSys)*, 2020. 8
- [3] Roshan Ayyalasomayajula, Aditya Arun, Chenfeng Wu, Sanatan Sharma, Abhishek Rajkumar Sethi, Deepak Vasisht, and Dinesh Bharadia. Deep learning based wireless localization for indoor navigation. In *ACM Annual International Conference on Mobile Computing and Networking (MobiCom)*, 2020. 1
- [4] Alexander Bergman, Petr Kellnhofer, Wang Yifan, Eric Chan, David Lindell, and Gordon Wetzstein. Generative Neural Articulated Radiance Fields. In *NeurIPS*, 2022. 3
- [5] Max Born and Emil Wolf. *Principles of Optics*. Cambridge University Press, 2013. 3
- [6] Anpei Chen, Zexiang Xu, Fuqiang Zhao, Xiaoshuai Zhang, Fanbo Xiang, Jingyi Yu, and Hao Su. MVSNeRF: Fast Generalizable Radiance Field Reconstruction from Multi-View Stereo. In *ICCV*, 2021. 3
- [7] Jianchuan Chen, Wentao Yi, Liqian Ma, Xu Jia, and Huchuan Lu. GM-NeRF: Learning Generalizable Model-based Neural Radiance Fields from Multi-view Images. In *CVPR*, 2023. 3
- [8] Shenchang Eric Chen and Lance Williams. View Interpolation for Image Synthesis. In *ACM SIGGRAPH*, 1993. 16
- [9] Xingyu Chen, Zihao Feng, Kun Qian, and Xinyu Zhang. Radio Frequency Ray Tracing with Neural Object Representation for Enhanced RF Modeling. In *CVPR*, pages 21339–21348, 2025. 3, 6
- [10] Weng Cho Chew. *Waves and Fields in Inhomogeneous Media*. John Wiley & Sons, 1999. 12
- [11] Zi-Ting Chou, Sheng-Yu Huang, I Liu, Yu-Chiang Frank Wang, et al. GSNeRF: Generalizable Semantic Neural Radiance Fields with Enhanced 3D Scene Understanding. In *CVPR*, 2024. 3
- [12] Cisco. Understand Site Survey Guidelines for WLAN Deployment, 2023. [Online]. 1
- [13] Cliff Drubin. Four Megatrends for 5G mmWave Technology in 2023 and Beyond. *Microwave Journal*, 66(3), 2023. 8
- [14] Esteban Egea-Lopez, Jose Maria Molina-Garcia-Pardo, Martine Lienard, and Pierre Degauque. Opal: An open source ray-tracing propagation simulator for electromagnetic characterization. *Plos one*, 16(11):e0260060, 2021. 1
- [15] Akshay Gadre, Revathy Narayanan, Anh Luong, Anthony Rowe, Bob Iannucci, and Swarun Kumar. Frequency Configuration for Low-Power Wide-Area Networks in a Heartbeat. In *USENIX Symposium on Networked Systems Design and Implementation (NSDI)*, 2020. 1
- [16] Mozhddeh Gheini, Xiang Ren, and Jonathan May. Cross-attention is all you need: Adapting pretrained transformers for machine translation. *arXiv preprint arXiv:2104.08771*, 2021. 20
- [17] Lidong Guo, Xuefei Ning, Yonggan Fu, Tianchen Zhao, Zhuoliang Kang, Jincheng Yu, Yingyan Celine Lin, and Yu Wang. Rad-NeRF: Ray-decoupled Training of Neural Radiance Field. In *NeurIPS*, 2024. 1
- [18] Kaiming He, Xiangyu Zhang, Shaoqing Ren, and Jian Sun. Deep residual learning for image recognition. In *CVPR*, 2016. 20
- [19] Haifeng Jia, Xinyi Chen, Yichen Wei, Yifei Sun, and Yibo Pi. Neural Reflectance Fields for Radio-Frequency Ray Tracing. In *IEEE Global Communications Conference (GLOBECOM)*, 2024. 1
- [20] Pushpendu Kar and Bhasker Dappuri. Site Survey and Radio Frequency Planning for the Deployment of Next Generation WLAN. In *IEEE International Conference on Wireless Communications, Signal Processing and Networking (WiSPNET)*, 2018. 1
- [21] Joseph B Keller. Geometrical Theory of Diffraction. *Journal of the Optical Society of America*, 52(2):116–130, 1962. 12
- [22] Bernhard Kerbl, Georgios Kopanas, Thomas Leimkühler, and George Drettakis. 3D Gaussian Splatting for Real-Time Radiance Field Rendering. In *ACM SIGGRAPH*, 2023. 3
- [23] Diederik P Kingma and Jimmy Ba. Adam: A method for stochastic optimization. In *ICLR*, 2015. 20
- [24] R.G. Kouyoumjian and P.H. Pathak. A Unifm Geometrical Theory of Diffraction for an Edge in a Perfectly Conducting Surface. *Proceedings of the IEEE*, 62(11):1448–1461, 1974. 1, 2, 20
- [25] ATTILA KOVARI. Synergizing 6G networks, IoT, and AI: Paving the way for next-generation intelligent ecosystems. *Journal of Engineering Science and Technology*, 20(1):114–128, 2025. 1
- [26] Pengfei Li, Jiaxin Fan, and Jianhong Wu. Exploring the key technologies and applications of 6G wireless communication network. *iScience*, 28(5), 2025. 1
- [27] Zechen Li, Lanqing Yang, Yiheng Bian, Hao Pan, Yongjian Fu, Yezhou Wang, Yi-Chao Chen, Guangtao Xue, and Ju Ren. Wideband RF Radiance Field Modeling Using Frequency-embedded 3D Gaussian Splatting. *arXiv preprint arXiv:2505.20714*, 2025. 3
- [28] Lingjie Liu, Jiatao Gu, Kyaw Zaw Lin, Tat-Seng Chua, and Christian Theobalt. Neural sparse voxel fields. In *NeurIPS*, 2020. 1
- [29] Yuan Liu, Sida Peng, Lingjie Liu, Qianqian Wang, Peng Wang, Christian Theobalt, Xiaowei Zhou, and Wenping Wang. Neural Rays for Occlusion-aware Image-based Rendering. In *CVPR*, 2022. 2, 3
- [30] Zhongyu Liu, Qi Yao, Quanqing Li, Lixin Guo, and Shuo Hu. Wireless Channel Model Based on Ray Tracing Algorithm in the Sea Environment. *International Journal of Antennas and Propagation*, 2024(1):3080895, 2024. 1
- [31] Haofan Lu, Christopher Vatheuer, Baharan Mirzasoleiman, and Omid Abari. NeWRF: A Deep Learning Framework for Wireless Radiation Field Reconstruction and Channel Prediction. In *ICML*, 2024. 1, 3, 6
- [32] Jiachen Lu, Hailan Shanbhag, and Haitham Al Hassanieh. GeRaF: Neural Geometry Reconstruction from Radio Frequency Signals. In *NeurIPS*, 2025. 3

- [33] Ricardo Martin-Brualla, Noha Radwan, Mehdi SM Sajjadi, Jonathan T Barron, Alexey Dosovitskiy, and Daniel Duckworth. NeRF in the Wild: Neural Radiance Fields for Unconstrained Photo Collections. In *CVPR*, 2021. 1
- [34] MATLAB. Indoor MIMO-OFDM Communication Link Using Ray Tracing, 2023. [Online]. 1, 6, 15
- [35] James Clerk Maxwell. *A Treatise on Electricity and Magnetism*. Oxford: Clarendon Press, 1873. 1
- [36] Quan Meng, Anpei Chen, Haimin Luo, Minye Wu, Hao Su, Lan Xu, Xuming He, and Jingyi Yu. GNeRF: GAN-based Neural Radiance Field without Posed Camera. In *ICCV*, 2021. 4
- [37] Ben Mildenhall, Pratul P Srinivasan, Matthew Tancik, Jonathan T Barron, Ravi Ramamoorthi, and Ren Ng. NeRF: Representing Scenes as Neural Radiance Fields for View Synthesis. *Communications of the ACM*, 65(1):99–106, 2021. 1, 2, 3
- [38] Cláudio Modesto, Lucas Mozart, Pedro Batista, André Cavalcante, and Aldebaro Klautau. Accelerating Ray Tracing-Based Wireless Channels Generation for Real-Time Network Digital Twins. *arXiv preprint arXiv:2504.09751*, 2025. 1
- [39] Alireza H Mohammadian, Vijaya Shankar, and William F Hall. Computation of electromagnetic scattering and radiation using a time-domain finite-volume discretization procedure. *Computer Physics Communications*, 68(1-3):175–196, 1991. 20
- [40] Han Na and Thomas F Eibert. A Huygens' Principle Based Ray Tracing Method for Diffraction Calculation. In *IEEE European Conference on Antennas and Propagation (EuCAP)*, 2022. 1, 2
- [41] Tribhuvanesh Orekondy, Pratik Kumar, Shreya Kadambi, Hao Ye, Joseph Soriaga, and Arash Behboodi. WiNeRT: Towards Neural Ray Tracing for Wireless Channel Modelling and Differentiable Simulations. In *ICLR*, 2023. 3, 6
- [42] Theodore S Rappaport. *Wireless communications: principles and practice*. Cambridge University Press, 1996. 12
- [43] Andreas Savvides, Chih-Chieh Han, and Mani B Strivastava. Dynamic fine-grained localization in Ad-Hoc networks of sensors. In *ACM Annual International Conference on Mobile Computing and Networking (MobiCom)*, 2001. 1
- [44] John Song, Lihao Zhang, Feng Ye, and Haijian Sun. Terahertz Spatial Wireless Channel Modeling with Radio Radiance Field. *arXiv preprint arXiv:2505.06277*, 2025. 8
- [45] Matthew Tancik, Vincent Casser, Xinchun Yan, Sabeek Pradhan, Ben Mildenhall, Pratul P Srinivasan, Jonathan T Barron, and Henrik Kretschmar. Block-NeRF: Scalable Large Scene Neural View Synthesis. In *CVPR*, 2022. 1, 3
- [46] Fengrui Tian, Shaoyi Du, and Yueqi Duan. MonoNeRF: Learning a Generalizable Dynamic Radiance Field from Monocular Videos. In *ICCV*, 2023. 3
- [47] Shuai Tong, Jiliang Wang, Jing Yang, Yunhao Liu, and Jun Zhang. Citywide LoRa Network Deployment and Operation: Measurements, Analysis, and Implications. In *ACM Conference on Embedded Networked Sensor Systems (SenSys)*, 2023. 1
- [48] Alex Trevithick and Bo Yang. GRF: Learning a General Radiance Field for 3D Representation and Rendering. In *ICCV*, 2021. 3
- [49] Shamsheer Ullah, Jianqiang Li, Jie Chen, Ikram Ali, Salabat Khan, Abdul Ahad, Farhan Ullah, and Victor CM Leung. A survey on emerging trends and applications of 5G and 6G to healthcare environments. *ACM Computing Surveys*, 57(4):1–36, 2024. 1
- [50] Ashish Vaswani, Noam Shazeer, Niki Parmar, Jakob Uszkoreit, Llion Jones, Aidan N Gomez, Łukasz Kaiser, and Illia Polosukhin. Attention is all you need. *Advances in Neural Information Processing Systems*, 30:6000–6010, 2017. 20
- [51] Qianqian Wang, Zhicheng Wang, Kyle Genova, Pratul P Srinivasan, Howard Zhou, Jonathan T Barron, Ricardo Martin-Brualla, Noah Snaveley, and Thomas Funkhouser. IBRNet: Learning Multi-View Image-Based Rendering. In *CVPR*, 2021. 2, 3
- [52] Zhou Wang, Alan C Bovik, Hamid R Sheikh, and Eero P Simoncelli. Image quality assessment: from error visibility to structural similarity. *IEEE transactions on image processing*, 13(4):600–612, 2004. 6
- [53] Chaozheng Wen, Jingwen Tong, Yingdong Hu, Zehong Lin, and Jun Zhang. WRF-GS: Wireless Radiation Field Reconstruction with 3D Gaussian Splatting. In *IEEE Conference on Computer Communications*, 2025. 3
- [54] P Wesling. Heterogeneous Integration Roadmap, 2021 Version, 2021. [Online]. 8
- [55] Po-zen Wong, Joel Koplik, and JP Tomanic. Conductivity and permeability of rocks. *Physical Review B*, 30(11):6606, 1984. 1, 7
- [56] Muyu Xu, Fangneng Zhan, Jiahui Zhang, Yingchen Yu, Xiaoqin Zhang, Christian Theobalt, Ling Shao, and Shijian Lu. WaveNeRF: Wavelet-based Generalizable Neural Radiance Fields. In *ICCV*, 2023. 3
- [57] Jiawei Yang, Marco Pavone, and Yue Wang. FreeNeRF: Improving Few-shot Neural Rendering with Free Frequency Regularization. In *CVPR*, 2023. 3
- [58] Kang Yang, Gaofeng Dong, Sijie Ji, Wan Du, and Mani Srivastava. GSRF: Complex-Valued 3D Gaussian Splatting for Efficient Radio-Frequency Data Synthesis. In *NeurIPS*, 2025. 3
- [59] Alex Yu, Vickie Ye, Matthew Tancik, and Angjoo Kanazawa. pixelnerf: Neural radiance fields from one or few images. In *CVPR*, 2021. 3
- [60] Zehao Yu, Anpei Chen, Binbin Huang, Torsten Sattler, and Andreas Geiger. Mip-Splatting: Alias-free 3D Gaussian Splatting. In *CVPR*, 2024. 3
- [61] Zhengqing Yun and Magdy F Iskander. Ray tracing for radio propagation modeling: Principles and applications. *IEEE Access*, 3:1089–1100, 2015. 1
- [62] Lihao Zhang, Haijian Sun, Samuel Berweger, Camillo Gentile, and Rose Qingyang Hu. RF-3DGS: Wireless Channel Modeling with Radio Radiance Field and 3D Gaussian Splatting. *arXiv preprint arXiv:2411.19420*, 2024. 3
- [63] Lihao Zhang, Zongtan Li, and Haijian Sun. RF-PGS: Fully-structured Spatial Wireless Channel Representation with Planar Gaussian Splatting. *arXiv preprint arXiv:2508.16849*, 2025. 3
- [64] Jun-Sheng Zhao and Weng Cho Chew. Integral Equation Solution of Maxwell's Equations from Zero Frequency to Mi-

crowave Frequencies. *IEEE transactions on antennas and propagation*, 48(10):1635–1645, 2000. [1](#)

- [65] Xiaopeng Zhao, Zhenlin An, Qingrui Pan, and Lei Yang. NeRF²: Neural Radio-Frequency Radiance Fields. In *ACM Annual International Conference on Mobile Computing and Networking (MobiCom)*, 2023. [1](#), [3](#), [5](#)
- [66] Haidong Zhu, Tianyu Ding, Tianyi Chen, Ilya Zharkov, Ram Nevatia, and Luming Liang. CaesarNeRF: Calibrated Semantic Representation for Few-shot Generalizable Neural Rendering. In *ECCV*, 2024. [3](#)

A. Proof of the Interpolation Theory in the RF Domain

We first present the mathematical proof, followed by empirical validation of the interpolation theory in the RF domain. Specifically, we show that the spatial spectrum $\mathbf{SS}(\mathbf{P})$ at any position \mathbf{P} can be approximated as a weighted combination of the spectra from its L -nearest neighbors $\mathcal{N}_L(\mathbf{P})$:

A.1. Mathematical Proof

We present a mathematical proof demonstrating that the spatial spectrum \mathbf{SS}_t at a target transmitter position \mathbf{P}_t can be approximated as a combination of spatial spectra $\{\mathbf{SS}_i\}_{i=1}^L$ corresponding to L neighboring transmitter positions $\{\mathbf{P}_i\}_{i=1}^L$. The proof is structured in three steps: a Taylor series expansion, a convex linear combination, and an error analysis.

Assumptions: The proof presupposes that transmitters and receivers equipped with isotropic antennas are placed in free 3D space, under the following two assumptions:

ASSUMPTION 1: A smooth propagation environment, wherein each transmitter position $\mathbf{P} \in \mathbb{R}^3$ is mapped to a corresponding spatial spectrum $\mathbf{SS} \in \mathbb{R}^{360 \times 90}$ through a function $\mathcal{T} : \mathbb{R}^3 \rightarrow \mathbb{R}^{360 \times 90}$. The mapping \mathcal{T} is assumed to be twice continuously differentiable with respect to the position $\mathbf{P} = (x, y, z)$. This regularity condition ensures that the spatial spectrum $\mathbf{SS} = \mathcal{T}(\mathbf{P})$ and its first- and second-order derivatives vary smoothly across the local region of \mathbf{P} , a standard postulate in physics-based analyses of wave propagation [10, 21].

For example, consider the Friis Free Space Propagation Equation [42], analogous to the mapping \mathcal{T} , where the received signal power S_{rx} at a receiver position \mathbf{P}_{rx} is given by (note that $S_{rx} \in \mathbb{R}$ is a scalar, whereas our setting involves a full spatial spectrum $\mathbf{SS} \in \mathbb{R}^{360 \times 90}$):

$$S_{rx} = S_{tx} \left(\frac{\lambda}{4\pi d} \right)^2, \quad \text{with } d = \|\mathbf{P}_{tx} - \mathbf{P}_{rx}\|$$

where S_{tx} is the transmitted power, λ is the wavelength, and d is the Euclidean distance between the transmitter at \mathbf{P}_{tx} and the receiver at \mathbf{P}_{rx} , which is a smooth function of position \mathbf{P} for $d > 0$. Since $S_{rx} \propto d^{-2}$, the received power also varies smoothly with respect to positional changes in \mathbf{P} .

While the Friis model yields a single scalar value, the mapping \mathcal{T} generalizes this concept to produce a spatial spectrum $\mathbf{SS} \in \mathbb{R}^{360 \times 90}$, representing signal power across all directions around the receiver, with smoothness similarly ensured by continuous variation in free space.

ASSUMPTION 2: We adopt the standard interpolation assumption in \mathbb{R}^3 : it is possible to identify neighboring positions $\{\mathbf{P}_i\}_{i=1}^L$ such that the target position \mathbf{P}_t lies within their convex hull, i.e.,

$$\sum_{i=1}^L w_i \mathbf{P}_i = \mathbf{P}_t$$

where the w_i are barycentric weights satisfying $w_i \geq 0$ and $\sum_{i=1}^L w_i = 1$.

Taylor Series Expansion of the Spatial Spectrum.

Objective: Derive the relationship between the spatial spectra at two proximate transmitter positions, \mathbf{P}_i and \mathbf{P}_j , where $\mathbf{P}_j = \mathbf{P}_i + \Delta\mathbf{P}_{ij}$ with $\Delta\mathbf{P}_{ij} = (x_j - x_i, y_j - y_i, z_j - z_i)$, by applying a Taylor series expansion under ASSUMPTION 1.

Statement:

$$\mathbf{SS}_j = \mathcal{T}(\mathbf{P}_i + \Delta\mathbf{P}_{ij}) = \mathbf{SS}_i + \nabla_{\mathbf{P}} \mathcal{T}(\mathbf{P}_i) \cdot \Delta\mathbf{P}_{ij} + \frac{1}{2} \Delta\mathbf{P}_{ij}^T \nabla_{\mathbf{P}}^2 \mathcal{T}(\mathbf{P}_i) \Delta\mathbf{P}_{ij} + \mathcal{O}(\|\Delta\mathbf{P}_{ij}\|^3)$$

Explanation:

- **Preliminaries:**

- Spectra \mathbf{SS}_i and \mathbf{SS}_j are defined through a mapping $\mathcal{T} : \mathbb{R}^3 \rightarrow \mathbb{R}^{360 \times 90}$, where $\mathbf{SS}_i = \mathcal{T}(\mathbf{P}_i)$ and $\mathbf{SS}_j = \mathcal{T}(\mathbf{P}_j)$, for transmitter positions $\mathbf{P}_i = (x_i, y_i, z_i) \in \mathbb{R}^3$ and $\mathbf{P}_j = \mathbf{P}_i + \Delta\mathbf{P}_{ij}$, with $\Delta\mathbf{P}_{ij}$ denoting the displacement vector between \mathbf{P}_i and \mathbf{P}_j .
- The magnitude of the displacement $\|\Delta\mathbf{P}_{ij}\|$ is assumed to be sufficiently small, ensuring that geometric perturbations remain minimal.

- **Terms:**

- $\nabla_{\mathbf{P}}\mathcal{J}(\mathbf{P}_i) = \left(\frac{\partial \mathcal{J}}{\partial x}, \frac{\partial \mathcal{J}}{\partial y}, \frac{\partial \mathcal{J}}{\partial z} \right) \in \mathbb{R}^{360 \times 90 \times 3}$: The gradient tensor, which quantifies the first-order sensitivity of the spatial spectrum to changes in the coordinates of \mathbf{P}_i .
- $\nabla_{\mathbf{P}}^2 \mathcal{J}(\mathbf{P}_i) \in \mathbb{R}^{360 \times 90 \times 3 \times 3}$: The Hessian tensor, comprising second-order partial derivatives and capturing the curvature of the spatial spectrum with respect to \mathbf{P}_i .
- $\mathcal{O}(\|\Delta \mathbf{P}_{ij}\|^3) \in \mathbb{R}^{360 \times 90}$: The remainder term, which encompasses third- and higher-order derivatives and becomes negligible when $\Delta \mathbf{P}_{ij}$ is sufficiently small.

Interpolating the Target Spectrum via Weighted Combination.

Objective: Estimate the spatial spectrum \mathbf{SS}_t at a target position $\mathbf{P}_t \in \mathbb{R}^3$ by blending the known spectra $\{\mathbf{SS}_i\}_{i=1}^L$ from nearby transmitter positions $\{\mathbf{P}_i\}_{i=1}^L \subset \mathbb{R}^3$.

Statement: Given the Taylor expansion from Step 1 and the barycentric weights (ASSUMPTION 2), the spatial spectrum at the target position \mathbf{P}_t can be approximated as:

$$\mathbf{SS}_t = \sum_{i=1}^L w_i \mathbf{SS}_i + \sum_{i=1}^L w_i \nabla_{\mathbf{P}} \mathcal{J}(\mathbf{P}_i) \cdot (\mathbf{P}_t - \mathbf{P}_i) + \mathcal{O}(\|\Delta \mathbf{P}\|^2)$$

where $\Delta \mathbf{P} = \max_i \|\mathbf{P}_t - \mathbf{P}_i\|$ denotes the maximum distance between the target position \mathbf{P}_t and its neighboring transmitter positions $\{\mathbf{P}_i\}_{i=1}^L$. Given the Lipschitz continuity of $\nabla_{\mathbf{P}} \mathcal{J}$ (which follows from the mapping function \mathcal{J} being twice continuously differentiable), the first-order term is bounded by $\mathcal{O}(\|\Delta \mathbf{P}\|^2)$, thereby simplifying the expression to:

$$\mathbf{SS}_t = \sum_{i=1}^L w_i \mathbf{SS}_i + \mathcal{O}(\|\Delta \mathbf{P}\|^2)$$

Explanation:

- **Construction:**

- For each neighbor \mathbf{P}_i , we use the Taylor expansion around \mathbf{P}_i from Step 1:

$$\mathbf{SS}_t = \mathbf{SS}_i + \nabla_{\mathbf{P}} \mathcal{J}(\mathbf{P}_i) \cdot (\mathbf{P}_t - \mathbf{P}_i) + \mathcal{O}(\|\mathbf{P}_t - \mathbf{P}_i\|^2)$$

This provides a local approximation of \mathbf{SS}_t when \mathbf{P}_t is close to \mathbf{P}_i .

- We combine these approximations using barycentric weights $\{w_i\}_{i=1}^L$, where $w_i \geq 0$, $\sum_{i=1}^L w_i = 1$, and $\sum_{i=1}^L w_i \mathbf{P}_i = \mathbf{P}_t$. The weighted estimate becomes:

$$\mathbf{SS}_t = \sum_{i=1}^L w_i \mathbf{SS}_i + \sum_{i=1}^L w_i \nabla_{\mathbf{P}} \mathcal{J}(\mathbf{P}_i) \cdot (\mathbf{P}_t - \mathbf{P}_i) + \sum_{i=1}^L w_i \mathcal{O}(\|\mathbf{P}_t - \mathbf{P}_i\|^2)$$

- **Simplification:**

- *Bounding the First-Order Term:* The barycentric property ensures:

$$\sum_{i=1}^L w_i (\mathbf{P}_t - \mathbf{P}_i) = \sum_{i=1}^L w_i \mathbf{P}_t - \sum_{i=1}^L w_i \mathbf{P}_i = \mathbf{P}_t - \mathbf{P}_t = \mathbf{0}$$

However, the gradients $\nabla_{\mathbf{P}} \mathcal{J}(\mathbf{P}_i)$ vary across positions \mathbf{P}_i . Since \mathcal{J} is twice differentiable, its gradient $\nabla_{\mathbf{P}} \mathcal{J}$ is Lipschitz continuous. Thus, we have:

$$\nabla_{\mathbf{P}} \mathcal{J}(\mathbf{P}_i) = \nabla_{\mathbf{P}} \mathcal{J}(\mathbf{P}_t) + \mathbf{E}_i, \quad \text{with} \quad \|\mathbf{E}_i\| \leq K_1 \|\mathbf{P}_t - \mathbf{P}_i\|$$

where K_1 is the Lipschitz constant of $\nabla_{\mathbf{P}} \mathcal{J}$, quantifying the maximum rate of change of the gradient, with $K_1 = 2K$ and $K = \frac{1}{2} \sup_{\mathbf{P} \in \text{conv}\{\mathbf{P}_i\}} \|\nabla_{\mathbf{P}}^2 \mathcal{J}(\mathbf{P})\|$ as defined in Step 3. Substituting into the first-order term, we obtain:

$$\sum_{i=1}^L w_i \nabla_{\mathbf{P}} \mathcal{J}(\mathbf{P}_i) \cdot (\mathbf{P}_t - \mathbf{P}_i) = \sum_{i=1}^L w_i [\nabla_{\mathbf{P}} \mathcal{J}(\mathbf{P}_t) + \mathbf{E}_i] \cdot (\mathbf{P}_t - \mathbf{P}_i)$$

This splits as:

$$\nabla_{\mathbf{P}} \mathcal{J}(\mathbf{P}_t) \cdot \sum_{i=1}^L w_i (\mathbf{P}_t - \mathbf{P}_i) + \sum_{i=1}^L w_i \mathbf{E}_i \cdot (\mathbf{P}_t - \mathbf{P}_i) = 0 + \sum_{i=1}^L w_i \mathbf{E}_i \cdot (\mathbf{P}_t - \mathbf{P}_i)$$

Bounding the error term:

$$\left\| \sum_{i=1}^L w_i \mathbf{E}_i \cdot (\mathbf{P}_t - \mathbf{P}_i) \right\| \leq \sum_{i=1}^L w_i \|\mathbf{E}_i\| \|\mathbf{P}_t - \mathbf{P}_i\| \leq K_1 \sum_{i=1}^L w_i \|\mathbf{P}_t - \mathbf{P}_i\|^2 \leq K_1 \|\Delta \mathbf{P}\|^2$$

where $\sum_{i=1}^L w_i = 1$. Therefore, the first-order term is bounded by $\mathcal{O}(\|\Delta \mathbf{P}\|^2)$.

– *Residual Error Term:* The higher-order terms are:

$$\sum_{i=1}^L w_i \mathcal{O}(\|\mathbf{P}_t - \mathbf{P}_i\|^2)$$

Since $\|\mathbf{P}_t - \mathbf{P}_i\| \leq \|\Delta \mathbf{P}\|$ and $\sum_{i=1}^L w_i = 1$, we have:

$$\sum_{i=1}^L w_i \mathcal{O}(\|\mathbf{P}_t - \mathbf{P}_i\|^2) \leq \mathcal{O}(\|\Delta \mathbf{P}\|^2)$$

– *Final Result:* Combining all terms:

$$\mathbf{SS}_t = \sum_{i=1}^L w_i \mathbf{SS}_i + \mathcal{O}(\|\Delta \mathbf{P}\|^2) + \mathcal{O}(\|\Delta \mathbf{P}\|^2) = \sum_{i=1}^L w_i \mathbf{SS}_i + \mathcal{O}(\|\Delta \mathbf{P}\|^2)$$

The error is quadratic in $\|\Delta \mathbf{P}\|$, meaning it decreases proportionally to the square of the maximum distance between the target position and its neighboring transmitters.

Quantifying the Interpolation Error.

Objective: Derive an upper bound on the interpolation error to assess the approximation accuracy.

Statement: The interpolation error $\epsilon = \left\| \mathbf{SS}_t - \sum_{i=1}^L w_i \mathbf{SS}_i \right\|$ satisfies the bound:

$$\epsilon \leq K \cdot \max_i \|\mathbf{P}_t - \mathbf{P}_i\|^2, \quad \text{with} \quad K = \frac{1}{2} \sup_{\mathbf{P} \in \text{conv}\{\mathbf{P}_i\}} \left\| \nabla_{\mathbf{P}}^2 \mathcal{J}(\mathbf{P}) \right\|$$

where K is a constant that depends on the second-order derivatives of the function \mathcal{J} , and encapsulates the maximum curvature of \mathcal{J} over the convex hull of the neighboring positions $\{\mathbf{P}_i\}_{i=1}^L$.

Explanation:

• **Derivation:**

– From Step 2, the interpolation error ϵ is expressed as:

$$\epsilon = \left\| \mathbf{SS}_t - \sum_{i=1}^L w_i \mathbf{SS}_i \right\| = \left\| \mathcal{O}(\|\Delta \mathbf{P}\|^2) \right\|$$

– $\mathcal{O}(\|\Delta \mathbf{P}\|^2)$ is bounded by the second derivatives of \mathcal{J} . By Taylor's theorem, for a twice continuously differentiable function \mathcal{J} , there exists a constant $K > 0$ such that:

$$\|\mathcal{J}(\mathbf{P}_t) - \mathcal{J}(\mathbf{P}_i) - \nabla_{\mathbf{P}} \mathcal{J}(\mathbf{P}_i) \cdot (\mathbf{P}_t - \mathbf{P}_i)\| \leq K \|\mathbf{P}_t - \mathbf{P}_i\|^2$$

where $K = \frac{1}{2} \sup_{\mathbf{P} \in \text{conv}\{\mathbf{P}_i\}} \left\| \nabla_{\mathbf{P}}^2 \mathcal{J}(\mathbf{P}) \right\|$ bounds the acceleration of the spatial spectrum's variation across the interpolation region. Smoother environments, those with gentler second-order changes, yield smaller K , tightening the error bound $\epsilon \leq K \cdot \|\Delta \mathbf{P}\|^2$. For example, in free-space propagation, K is negligible, whereas near obstacles, where signal strength fluctuates rapidly, K grows significantly.

- * $\nabla_{\mathbf{P}}^2 \mathcal{J}(\mathbf{P})$ is the *Hessian matrix* of \mathcal{J} at \mathbf{P} , quantifying how sensitively the spectrum changes in response to second-order variations in the transmitter coordinates.
 - * $\|\nabla_{\mathbf{P}}^2 \mathcal{J}(\mathbf{P})\|$ denotes the *operator norm* of the Hessian, a scalar measure of its "magnitude," representing the maximum rate of curvature of \mathcal{J} in any direction.
 - * $\sup_{\mathbf{P} \in \text{conv}\{\mathbf{P}_i\}}$ takes the *supremum* (least upper bound) of the Hessian norm over all points in the convex hull of the neighboring positions $\{\mathbf{P}_i\}$. This represents the worst-case curvature of \mathcal{J} within the local interpolation region.
- Summing over all neighbors' spatial spectra with barycentric weights w_i , and noting that $\sum_{i=1}^L w_i = 1$, the total error satisfies:

$$\epsilon \leq \sum_{i=1}^L w_i \cdot K \|\mathbf{P}_t - \mathbf{P}_i\|^2 \leq K \cdot \max_i \|\mathbf{P}_t - \mathbf{P}_i\|^2$$

• **Intuition:**

- **Interpretability of K :** The constant K directly quantifies the worst-case curvature of \mathcal{J} over the interpolation region, as governed by the Hessian $\nabla_{\mathbf{P}}^2 \mathcal{J}$. In free-space propagation (low curvature, small K), the bound tightens significantly, whereas near obstacles or multipath-rich environments (high curvature, large K), the error grows predictably. This ties the theoretical guarantee to physically observable phenomena, ensuring the result is not merely abstract but grounded in wave physics.
- **Scope of the Error Bound:** The derived bound applies specifically to the linear convex combination of neighboring spectra, as defined by barycentric weights. While this provides a foundational guarantee for basic linear interpolation, the *GRaF* architecture extends beyond this linear regime. By integrating a neural network, *GRaF* learns nonlinear corrections to the weighted spectral average, capturing higher-order correlations and environmental discontinuities (e.g., diffraction, reflection, scattering) that the linear model cannot represent. Thus, the proven bound serves as a baseline for the worst-case error in linear neighbor spatial spectrum interpolation.

A.2. Empirical Validation

The rationale is based on two observations highlighted in this subsection. First, for a given target transmitter, neighboring transmitters typically traverse similar propagation paths, *i.e.*, they pass through many common voxels within the scene. Second, the spectrum for the target transmitter can be perceived as an interpolation of the spectra from its neighbors. Consequently, leveraging the spectra from these neighbors facilitates the spectrum generation for the target transmitter, thereby improving the generalization ability as long as neighbor data is available. We conduct two empirical experiments to demonstrate these two observations.

Observation #1. In a conference room, as depicted in Figure 8a, we position the RX at a fixed location and place TX1 and TX2 at two closely situated positions. We utilize the MATLAB ray tracing simulation [34] to conduct RF ray tracing analysis. This software calculates all the propagation paths between the transmitters and the receiver. For brevity, we present one path from either TX1 or TX2 to the RX in Figure 8a. It is evident that the starting and reflection positions of the two paths are very close, and they both terminate at the RX.

For a more general case, we generate 500 pairs of closely positioned TX1 and TX2, execute the RF Insite ray tracing algorithm for each pair, and then compare the distances between the reflection points of their corresponding paths. Figure 8a shows that approximately 80% of the distances between reflection points are less than 0.1 m. Given their close starting positions, proximate reflection points, and identical end positions, these factors collectively indicate a similar propagation path. Moreover, assuming the voxel size equals the wavelength, such as 0.13 m for 2.4 GHz WiFi, the path differences are typically less than the voxel size. Therefore, the propagation paths for closely positioned transmitters typically pass through many common voxels.

Observation #2. Given that closely positioned transmitters pass through many common voxels, their spectra may exhibit some correlations. To verify this, we conduct an experiment using RFID dataset (details in Section Experiments). For each transmitter and its corresponding spectrum, we identify the 6 closest positions of other transmitters as its neighbors. We then assign a weight matrix to each neighbor; since the spectrum size is (360, 90), each weight matrix is also (360, 90), with every pixel of the spectrum assigned a specific weight. Using each neighbor's spectrum and its assigned weight matrix, we perform a weighted summation of all neighbors' spectra to predict the target transmitter's spectrum. We employ the MSE loss to train the 6 weight matrices over 200 iterations for each target transmitter. Once trained, we compare the generated spatial spectrum with the ground truth spectrum.

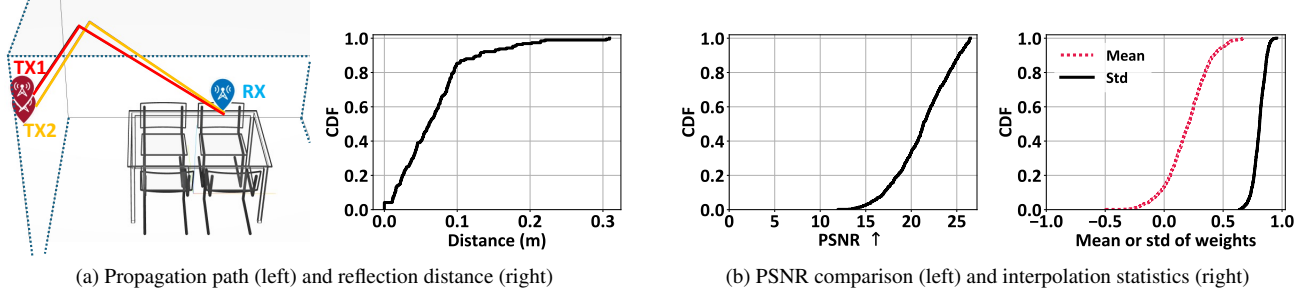


Figure 8. (Left) Propagation path differences and reflection distance between two transmitters (TXs) and a receiver (RX). (Right) PSNR when using neighbors’ spectra and statistics of the interpolation matrix.

Figure 8b illustrates that an average PSNR of 20.5 dB with a standard deviation of 4.1 dB is achieved for the interpolated spectra. To understand what the value of 20.5 dB represents, refer to the second row, first column of Figure 4, which displays a PSNR of 19.5 dB between two spatial spectra. Visually, the similarity between them is apparent. Thus, an average PSNR of 20.5 dB suggests that the neighbors’ spectra are indeed closely related to the target transmitter’s spectrum. Hence, the target transmitter’s spectrum can be viewed as an interpolation of the spectra of its neighbors. Explaining this phenomenon from a broader perspective, novel view synthesis in the context of visible light can be achieved by interpolating between images captured from different camera poses and views [8]. Similarly, RF signals may also exhibit such properties. Because visible light and RF signals are both forms of electromagnetic waves, they might share underlying interpolation characteristics, despite their differences in propagation behaviors.

You might wonder whether this interpolation method could be directly applied to synthesize spectra for a target transmitter. The answer is NO. First, although the generated spectrum shows promise, it is not sufficiently accurate. Second, the weight matrices are highly dependent on the transmitter positions. A set of weight matrices from one transmitter cannot be applied to another transmitter. We normalize all learned weight matrices for all transmitters and present their mean and standard deviation in Figure 8b. It can be observed that the values range from -1.0 to 1.0 , covering all possible values. Thus, the values of the weight matrix are highly dynamic, and a single set of weight matrices cannot be used for other transmitters.

B. Derivation of the Received Signal in Neural Ray Tracing

Objective.

The objective is to derive the expression for the received signal y_r in the neural ray tracing algorithm:

$$y_r = \sum_{s=1}^S \left(\prod_{j=1}^{s-1} a(\mathbf{x}_j, \alpha, \beta) \right) s(\mathbf{x}_s, \alpha, \beta) \cdot \frac{\lambda}{4\pi d_s} e^{-j \frac{2\pi f d_s}{c}}. \quad (18)$$

It models the RF signal received at the receiver by aggregating contributions from all sampled points along the ray, considering both attenuation and phase shifts introduced during propagation.

Maxwell’s Equations and the Wave Equation.

We begin with Maxwell’s equations, which govern electromagnetic wave propagation. In free space (*i.e.*, no charges or currents), the electric field \mathbf{E} satisfies the wave equation. Taking the curl of Faraday’s law and applying the constitutive relations, we derive the wave equation:

$$\nabla^2 \mathbf{E} + k^2 \mathbf{E} = 0,$$

where:

- ∇^2 is the Laplacian operator, representing spatial changes in the field,
- $k = \frac{2\pi f}{c} = \frac{2\pi}{\lambda}$ is the wave number,
- f is the signal frequency,
- c is the speed of light,
- λ is the wavelength.

This is the Helmholtz equation, which describes how electromagnetic waves propagate through space. For clarity, we simplify the analysis to a scalar field, representing a single component of \mathbf{E} .

Green's Function: Modeling a Point Source.

To solve the Helmholtz equation for a point source (such as a radiating point along a ray), we employ the Green's function. For a source located at position \mathbf{x}' , the resulting field at position \mathbf{x} is:

$$G(\mathbf{x}, \mathbf{x}') = \frac{e^{-jk\|\mathbf{x}-\mathbf{x}'\|}}{4\pi\|\mathbf{x}-\mathbf{x}'\|},$$

where:

- **Physical Meaning:** Represents a spherical wave emanating from \mathbf{x}' .
- **Terms:**
 - $e^{-jk\|\mathbf{x}-\mathbf{x}'\|}$: Phase shift induced by traveling the distance $\|\mathbf{x}-\mathbf{x}'\|$,
 - $\frac{1}{4\pi\|\mathbf{x}-\mathbf{x}'\|}$: Amplitude decay due to spherical spreading,
 - $k = \frac{2\pi}{\lambda}$: Wave number, relating phase to wavelength.

This serves as the fundamental block for modeling wave propagation from a single point source.

Ray Tracing: Discretizing the Path.

In ray tracing, the signal path is modeled as a series of discrete points \mathbf{x}_s , where $s = 1, 2, \dots, S$. Each point acts as a secondary source, radiating its own contribution to the received signal. The field at the receiver \mathbf{P}_{rx} from a point \mathbf{x}_s is expressed as:

$$E_s(\mathbf{P}_{\text{rx}}) = s(\mathbf{x}_s, \alpha, \beta) \cdot \frac{e^{-jk d_s}}{4\pi d_s},$$

where:

- $s(\mathbf{x}_s, \alpha, \beta)$: The complex signal (amplitude and phase) emitted or scattered at \mathbf{x}_s , dependent on position and parameters α, β ,
- $d_s = \|\mathbf{x}_s - \mathbf{P}_{\text{rx}}\|$: The Euclidean distance from \mathbf{x}_s to the receiver,
- $\frac{e^{-jk d_s}}{4\pi d_s}$: The Green's function applied over the path distance, accounting for spherical wave spreading and phase shift.

The signal at \mathbf{x}_s radiates as a spherical wave, and this formulation computes its contribution to the total field strength at the receiver.

Adding Path Attenuation.

As the signal propagates from the transmitter to \mathbf{x}_s , it undergoes interactions such as reflections and absorptions at earlier points \mathbf{x}_j , where $j = 1, 2, \dots, s-1$. We model this cumulative effect as:

$$\prod_{j=1}^{s-1} a(\mathbf{x}_j, \alpha, \beta),$$

- **Physical Meaning:** Each $a(\mathbf{x}_j, \alpha, \beta)$ is a complex factor that represents attenuation (magnitude less than 1) and phase shift induced by the material or obstacle at \mathbf{x}_j .
- **Multiplicative Nature:** These factors multiply sequentially because each segment modifies the signal as it progresses through the path.

Thus, the contribution from the sampled point \mathbf{x}_s to the received signal becomes:

$$\left(\prod_{j=1}^{s-1} a(\mathbf{x}_j, \alpha, \beta) \right) s(\mathbf{x}_s, \alpha, \beta) \cdot \frac{e^{-jk d_s}}{4\pi d_s}.$$

This expression incorporates both the path attenuation effects accumulated from previous points and the radiated field from \mathbf{x}_s , considering distance-based decay and phase shift as modeled by the Green's function.

Summing All Contributions.

The received signal y_r is obtained by summing the contributions from all S sampled points along the ray path:

$$y_r = \sum_{s=1}^S \left(\prod_{j=1}^{s-1} a(\mathbf{x}_j, \alpha, \beta) \right) s(\mathbf{x}_s, \alpha, \beta) \cdot \frac{e^{-jk d_s}}{4\pi d_s}.$$

- **Why Sum?** In wave propagation, fields from multiple sources superpose linearly, assuming linearity of the medium.
- **Adjustment:** Substitute $k = \frac{2\pi f}{c}$, and recognize that $\frac{1}{4\pi d_s}$ can be scaled by the wavelength λ for dimensional consistency:

$$y_r = \sum_{s=1}^S \left(\prod_{j=1}^{s-1} a(\mathbf{x}_j, \alpha, \beta) \right) s(\mathbf{x}_s, \alpha, \beta) \cdot \frac{\lambda}{4\pi d_s} e^{-j \frac{2\pi f d_s}{c}}.$$

This formulation links electromagnetic theory with the neural ray tracing model, enabling accurate RF signal prediction by accounting for path attenuation, phase shifts, and spherical spreading.

C. Proof of Loss Function

We prove that the optimization problem for maximizing the log-likelihood of the spatial spectrum:

$$\Theta^* = \arg \max_{\Theta} \log p(\mathbf{SS}_{\Theta} | \mathcal{N}_L, \mathbf{P}),$$

where:

$$\log p(\mathbf{SS}_{\Theta} | \mathcal{N}_L, \mathbf{P}) = \log \int \prod_{r=1}^Q p(\mathbf{SS}(r) | \mathbf{Z}, \mathbf{P}) p(\mathbf{Z} | \mathcal{N}_L) d\mathbf{Z},$$

can be reformulated as minimizing the ℓ_2 reconstruction loss:

$$\Theta^* = \arg \min_{\Theta} \sum_{r=1}^Q \left\| \mathbf{SS}(r) - \hat{\mathbf{SS}}_{\Theta}(r) \right\|^2,$$

given that \mathbf{Z} is deterministically computed by the latent RF radiance field as $\mathbf{Z} = \mathcal{T}_{\Psi}(\mathcal{N}_L, \mathbf{P})$.

Simplifying the Integral with Deterministic \mathbf{Z} .

The likelihood involves an integral over the latent variable \mathbf{Z} :

$$p(\mathbf{SS}_{\Theta} | \mathcal{N}_L, \mathbf{P}) = \int \prod_{r=1}^Q p(\mathbf{SS}(r) | \mathbf{Z}, \mathbf{P}) p(\mathbf{Z} | \mathcal{N}_L) d\mathbf{Z}.$$

Since \mathbf{Z} is deterministically computed by the function \mathcal{T}_{Ψ} , *i.e.*, $\mathbf{Z} = \mathcal{T}_{\Psi}(\mathcal{N}_L, \mathbf{P})$, the conditional distribution $p(\mathbf{Z} | \mathcal{N}_L)$ is a Dirac delta function:

$$p(\mathbf{Z} | \mathcal{N}_L) = \delta(\mathbf{Z} - \mathcal{T}_{\Psi}(\mathcal{N}_L, \mathbf{P})).$$

Substituting this into the integral:

$$p(\mathbf{SS}_{\Theta} | \mathcal{N}_L, \mathbf{P}) = \int \prod_{r=1}^Q p(\mathbf{SS}(r) | \mathbf{Z}, \mathbf{P}) \delta(\mathbf{Z} - \mathcal{T}_{\Psi}(\mathcal{N}_L, \mathbf{P})) d\mathbf{Z}.$$

Using the property of the Dirac delta function:

$$\int f(\mathbf{Z}) \delta(\mathbf{Z} - \mathbf{Z}_0) d\mathbf{Z} = f(\mathbf{Z}_0),$$

the integral evaluates to the integrand at $\mathbf{Z} = \mathcal{T}_\Psi(\mathcal{N}_L, \mathbf{P})$:

$$p(\mathbf{SS}_\Theta | \mathcal{N}_L, \mathbf{P}) = \prod_{r=1}^Q p(\mathbf{SS}(r) | \mathcal{T}_\Psi(\mathcal{N}_L, \mathbf{P}), \mathbf{P}).$$

Taking the logarithm:

$$\log p(\mathbf{SS}_\Theta | \mathcal{N}_L, \mathbf{P}) = \log \prod_{r=1}^Q p(\mathbf{SS}(r) | \mathcal{T}_\Psi(\mathcal{N}_L, \mathbf{P}), \mathbf{P}) = \sum_{r=1}^Q \log p(\mathbf{SS}(r) | \mathcal{T}_\Psi(\mathcal{N}_L, \mathbf{P}), \mathbf{P}).$$

Thus, the optimization problem becomes:

$$\Theta^* = \arg \max_{\Theta} \sum_{r=1}^Q \log p(\mathbf{SS}(r) | \mathcal{T}_\Psi(\mathcal{N}_L, \mathbf{P}), \mathbf{P}).$$

Modeling the Conditional Likelihood.

To proceed, we specify the conditional likelihood $p(\mathbf{SS}(r) | \mathbf{Z}, \mathbf{P})$. In supervised learning tasks involving continuous outputs, such as reconstructing spatial spectra, it is standard to assume the observations follow a Gaussian distribution centered at the model's prediction. Let $\hat{\mathbf{S}}\mathbf{S}_\Theta(r)$ denote the predicted spatial spectrum for ray r , parameterized by Θ . We assume:

$$p(\mathbf{SS}(r) | \mathbf{Z}, \mathbf{P}) = \mathcal{N}(\mathbf{SS}(r) | \hat{\mathbf{S}}\mathbf{S}_\Theta(r), \sigma^2),$$

where \mathcal{N} denotes a Gaussian distribution with mean $\hat{\mathbf{S}}\mathbf{S}_\Theta(r)$ and variance σ^2 , and $\mathbf{Z} = \mathcal{T}_\Psi(\mathcal{N}_L, \mathbf{P})$. The Gaussian probability density function is given by:

$$p(\mathbf{SS}(r) | \mathbf{Z}, \mathbf{P}) = \frac{1}{\sqrt{2\pi\sigma^2}} \exp\left(-\frac{1}{2\sigma^2} \|\mathbf{SS}(r) - \hat{\mathbf{S}}\mathbf{S}_\Theta(r)\|^2\right).$$

Taking the logarithm:

$$\log p(\mathbf{SS}(r) | \mathbf{Z}, \mathbf{P}) = \log\left(\frac{1}{\sqrt{2\pi\sigma^2}}\right) - \frac{1}{2\sigma^2} \|\mathbf{SS}(r) - \hat{\mathbf{S}}\mathbf{S}_\Theta(r)\|^2.$$

Thus we have:

$$\log p(\mathbf{SS}(r) | \mathbf{Z}, \mathbf{P}) = -\frac{1}{2} \log(2\pi\sigma^2) - \frac{1}{2\sigma^2} \|\mathbf{SS}(r) - \hat{\mathbf{S}}\mathbf{S}_\Theta(r)\|^2.$$

Summing over all Q rays:

$$\sum_{r=1}^Q \log p(\mathbf{SS}(r) | \mathcal{T}_\Psi(\mathcal{N}_L, \mathbf{P}), \mathbf{P}) = \sum_{r=1}^Q \left[-\frac{1}{2} \log(2\pi\sigma^2) - \frac{1}{2\sigma^2} \|\mathbf{SS}(r) - \hat{\mathbf{S}}\mathbf{S}_\Theta(r)\|^2 \right].$$

This can be written as:

$$-\frac{Q}{2} \log(2\pi\sigma^2) - \frac{1}{2\sigma^2} \sum_{r=1}^Q \|\mathbf{SS}(r) - \hat{\mathbf{S}}\mathbf{S}_\Theta(r)\|^2.$$

Equivalence to ℓ_2 Loss Minimization.

To maximize the log-likelihood:

$$\Theta^* = \arg \max_{\Theta} \left[-\frac{Q}{2} \log(2\pi\sigma^2) - \frac{1}{2\sigma^2} \sum_{r=1}^Q \|\mathbf{SS}(r) - \hat{\mathbf{S}}\mathbf{S}_\Theta(r)\|^2 \right].$$

The first term, $-\frac{Q}{2} \log(2\pi\sigma^2)$, is constant with respect to Θ , as σ^2 is fixed. Thus, maximizing the log-likelihood is equivalent to minimizing the negative of the second term:

$$\Theta^* = \arg \min_{\Theta} \frac{1}{2\sigma^2} \sum_{r=1}^Q \|\mathbf{SS}(r) - \hat{\mathbf{S}}\mathbf{S}_\Theta(r)\|^2.$$

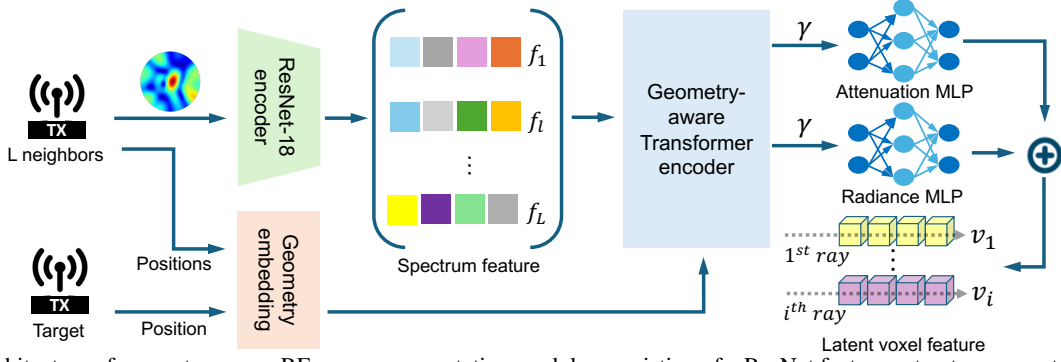


Figure 9. Architecture of geometry-aware RF scene representation module, consisting of a ResNet feature extractor, geometry embedding, a Transformer encoder, and two MLPs, where a circle with a plus symbol signifies concatenation.

Since $\frac{1}{2\sigma^2}$ is a positive constant, it does not affect the optimization. Therefore, the optimization simplifies to:

$$\Theta^* = \arg \min_{\Theta} \sum_{r=1}^Q \left\| \mathbf{SS}(r) - \hat{\mathbf{SS}}_{\Theta}(r) \right\|^2.$$

This loss encourages *GRaF* to accurately reconstruct the spatial spectrum while learning contextual latent features from neighboring transmitters’ spatial spectra that generalize across diverse scenes.

D. Implementation Details

Training. *GRaF* is trained end-to-end using the L2 loss function, computed per ray as the ray tracing algorithm processes each ray individually, to minimize the difference between the predicted and ground truth signal power. Training is optimized with the Adam optimizer [23], starting with an initial learning rate of 5.0×10^{-4} , which decays exponentially. *GRaF* is trained for 300,000 steps over approximately 15 hours, with 5, 120 rays sampled from the spatial spectrum at each step.

Neighbor Selection Strategy. We select neighbors based on Euclidean distance between transmitter positions, which is directly aligned with our interpolation theory: the approximation error is bounded by $K \Delta P^2$, where ΔP is the maximum distance to the selected neighbors and K characterizes the environment curvature. This implies that the spatial proximity of neighbors (quantified by ΔP) and the environment curvature K primarily determine synthesis quality.

To ensure robustness across both dense and sparse regions, we randomly sample $L \in [3, 10]$ for each target transmitter. This encourages the model to learn stable geometric relationships under diverse neighborhood configurations, rather than overfitting to a fixed neighbor count. During testing, neighbors are selected from the training split of the target scene to avoid information leakage. Appendix §E.3 analyzes their impact on synthesis quality.

Because KNN, KNN-DL, and *GRaF* rely exclusively on neighbors from unseen scenes at test time, we fine-tune *NeRF*² on the same data to ensure a fair comparison, as *NeRF*² otherwise requires scene-specific training.

Positional encoding. For the 3D coordinates of transmitter positions, neighbors’ positions, and ray positions and directions, we transform these low-dimensional coordinates into high-dimensional representations using the Position Embedding function [50], with 10 frequency bands in all experiments. This expands the 3D coordinates from 3 to $3 + 3 \times 10 \times 2 = 63$ dimensions. In cross-scene experiments, where each transmitter position includes 3D coordinates and a scene index, the 4D coordinates are expanded to $4 + 4 \times 10 \times 2 = 84$ dimensions. This transformation allows the network to distinguish identical coordinates across different scenes.

Voxel Size. The voxel size is consistently set to the wireless signal’s wavelength, aligning with the physics of RF propagation. Since phenomena like reflection and diffraction occur at the wavelength scale, this choice ensures that the model captures fine-grained interactions. This design is validated by prior work [24], which solves Maxwell’s equations using a finite-volume discretization matched to the electromagnetic wavelength [39].

Radiance Field. Figure 9 illustrates the architecture of our RF radiance field. It comprises a ResNet-18 feature encoder [18], geometry embedding, a geometry-aware Transformer encoder with a cross-attention mechanism [16], and two MLPs.

To extract compact spectral features from the neighboring spectra, we utilize a ResNet-18 encoder with filter settings of 64, 128, 256, and 512 [18]. Both the RF scene representation and the neural ray tracing algorithm are implemented with a Transformer-based architecture. A typical Transformer consists of multiple stacked blocks; each block contains an attention

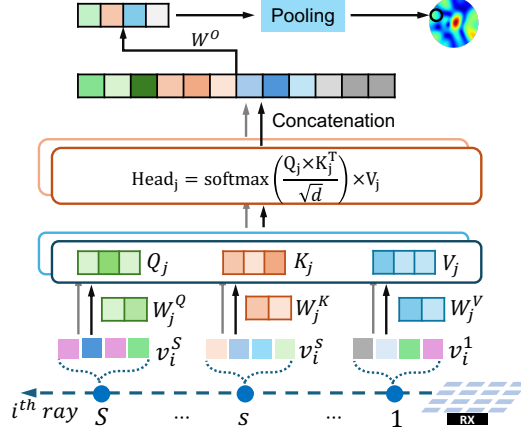


Figure 10. Architecture of the neural-driven ray tracing algorithm, where S voxels are sampled along the i -th ray (RX: receiver).

layer, followed by a residual connection from the input to the post-attention layer, and then layer normalization (LayerNorm). Subsequently, a Feed-Forward Network (FFN) with Rectified Linear Unit (ReLU) activation is applied. This is followed by another residual connection from the output of the first LayerNorm to the output of the ReLU, and the sequence concludes with a second LayerNorm.

The Transformers in both the RF scene representation and the ray tracing algorithm consist of two stacked blocks, each with a hidden dimension of 16, matching the voxel latent feature dimension d . However, there are two key differences between these two Transformers. First, the attention mechanisms differ. The scene representation module incorporates a single-headed cross-attention layer, while the ray tracing Transformer uses a multi-headed self-attention layer. Second, the handling of token sequential information varies. In the scene representation module, the sequential order of spectrum features is not critical, as the focus lies in the differences between pairs of features. Therefore, the index of the spectrum features is not considered. On the other hand, in the ray tracing algorithm, the sequential information of voxels along a ray is essential, as it directly impacts the calculation of attention weights. Therefore, the index of each voxel along the ray is incorporated.

Ray Tracing. Figure 10 illustrates the proposed neural-driven ray tracing algorithm. It utilizes a standard transformer encoder architecture, but here we focus on the core attention mechanism. Along the ray, S voxels are sampled, and their latent features $\{\mathbf{v}^s\}_{s=1,\dots,S}$ are extracted, with each \mathbf{v}^s treated as a token. The attention scores are computed using the softmax function applied to the scaled product of the Query matrix Q and Key matrix K , where d is the voxel feature dimension. The scores weight the Value matrix V , resulting in an aggregated latent voxel feature across all S voxels:

$$\text{Attention}(\mathbf{Q}, \mathbf{K}, \mathbf{V}) = \text{softmax}\left(\frac{\mathbf{Q}\mathbf{K}^T}{\sqrt{d}}\right) \mathbf{V}$$

Each voxel feature implicitly encodes the real and imaginary parts of the signal and attenuation, allowing attention scores to capture their complex relationships. Among these, all possible pairwise combinations total $\binom{4+2-1}{2} = 10$, leading to the use of ten attention heads in the transformer to effectively model these dynamics. Each head is equipped with distinct learnable projection matrices \mathbf{W}_Q^j , \mathbf{W}_K^j , and \mathbf{W}_V^j , where j indexes the head from 1 to 10. The output of each head, Head_j , is concatenated into a new feature, which is then multiplied by another learnable projection matrix \mathbf{W}_o to produce the predicted feature for each voxel along the current i -th ray. Finally, mean pooling is performed over all voxels along the ray, and the pooled feature vector is mapped to the real and imaginary parts of the received signal. The amplitude of the resulting signal is calculated as the predicted signal power for the ray.

E. Experimental Results

E.1. Why Simulation Data

GRaF is designed to achieve spatial generalization, enabling adaptation to changes in scene layouts, object placements, and environmental configurations without retraining for each new scene. Simulation offers the precise control necessary for evaluating this capability. Using tools such as Blender to manipulate high-fidelity CAD models, we can systematically modify scene geometry (for example, adding or removing chairs and tables as in ConferenceV1–V3 and OfficeV1–V3) while eliminating confounding factors such as human movement, electromagnetic interference, hardware noise, or temporal drift.

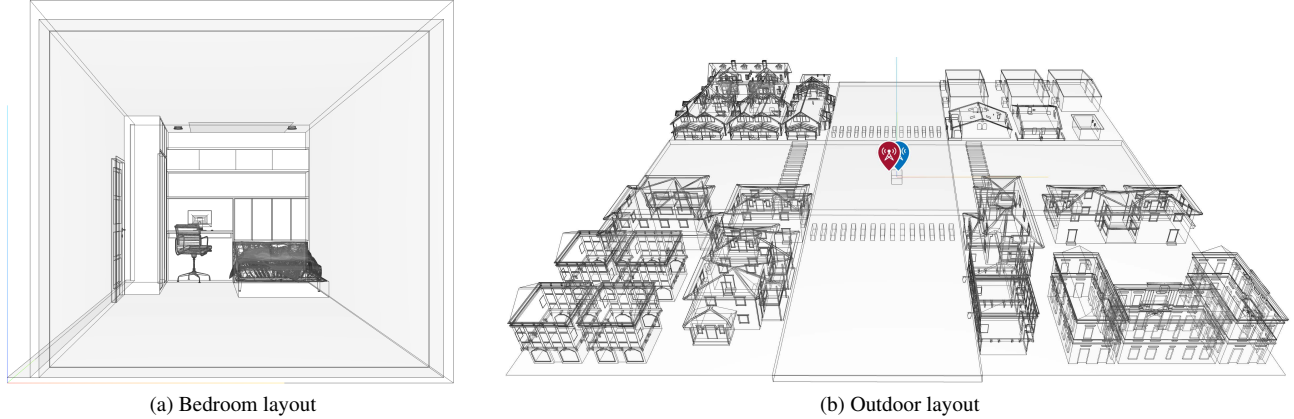


Figure 11. Visualization of two extra layouts for evaluation: a Bedroom scene and an Outdoor scene.

This level of control is essential for rigorously isolating spatial generalization, as demonstrated in our cross-scene experiments where models trained on one layout version (*e.g.*, ConferenceV1) are evaluated on unseen variants (*e.g.*, ConferenceV2/V3) containing structural changes.

Real-world data collection introduces many uncontrolled variables that evolve over time, including changes in occupancy, temperature, humidity, and multipath conditions. Such variability is better suited for studying temporal adaptation or dynamic-scene modeling frameworks (for example, deformable or time-varying NeRFs), rather than spatial generalization.

In contrast, MATLAB-based ray tracing provides high-quality, noise-free supervision for evaluating spectrum synthesis. These simulations incorporate accurate CAD geometry and material properties to model RF propagation phenomena, including reflection, diffraction, scattering, and path loss. The CAD model effectively serves as a physically grounded proxy for the real environment, ensuring that the generated spectra remain geometrically aligned and consistent with Maxwellian propagation behaviors. This controlled and high-fidelity setting is crucial for validating theoretical contributions such as our Spectrum Interpolation Theorem (Theorem 1) and for enabling fair comparison to baseline methods.

To complement simulations and validate real-world applicability, we also evaluate on the RFID dataset, which contains 6,123 real measurements collected at 915 MHz using a 4×4 antenna array. *GRaF* achieves state-of-the-art performance on this dataset, demonstrating compatibility with hardware-collected signals.

Trade-off Between Simulation Quality and Computational Overhead. MATLAB ray tracing provides highly accurate spectra by leveraging detailed CAD models and physics-based rendering. However, this accuracy comes with substantial overhead. Constructing a realistic CAD model requires specialized scanning systems (for example, a \sim \$75K LiDAR scanner) along with significant expert effort to refine geometry and assign accurate material properties. Simulation is also computationally expensive: generating a single spectrum requires an average of 59.5 seconds, resulting in 95.5 hours to generate 5,782 spectra for the bedroom and outdoor layouts (Appendix E.2). This expense creates scalability challenges when building large datasets or iterating over multiple scene variants.

In contrast, *GRaF* operates without any CAD models or pre-existing scene geometry. It requires only transmitter positions and collected spatial spectra, both of which can be obtained using commodity wireless hardware. For example, on the RFID dataset, *GRaF* trains in roughly 15 hours on a single GPU and achieves competitive synthesis quality (21.94 PSNR and 0.766 SSIM in Table 1) alongside strong cross-scene generalization. These characteristics make *GRaF* practical for real deployments such as WiFi-based localization, RFID sensing, and network planning, where rapid adaptation to new environments is essential. By removing the need for expensive simulations or geometry reconstruction, *GRaF* lowers the barrier to widespread adoption while maintaining high performance. This is further supported by its improvement over NeRF2, achieving up to a 50.4% LPIPS reduction across simulated and real datasets.

E.2. Generalization to Unseen Layouts

Extending the generalization analysis in §5.4, we further evaluate the generalization ability of *GRaF* and *NeRF*² (both trained on the Conference and Office layouts) on three additional and structurally distinct scenes:

- **Bedroom** (Figure 11a): $23.6 \text{ ft} \times 48.9 \text{ ft} \times 20.2 \text{ ft}$, with spatial spectra collected at 2700 transmitter locations.
- **Outdoor** (Figure 11b): $158.5 \text{ ft} \times 154.6 \text{ ft} \times 33.5 \text{ ft}$, with spatial spectra collected at 3082 transmitter locations.
- **RFID (Real-World)**: described in §5.1, covering $76.5 \text{ ft} \times 81.9 \text{ ft} \times 9.6 \text{ ft}$.

These three settings introduce diverse spatial characteristics: the *Bedroom* scene captures confined, multipath-rich indoor

Table 7. Performance on bedroom scene.

Model	MSE↓	LPIPS↓	PSNR↑	SSIM↑
KNN-DL	0.389	0.550	4.08	0.140
NeRF ²	0.429	0.575	3.68	0.160
<i>GRaF</i>	0.114	0.390	9.43	0.204

Table 9. RFID performance without fine-tuning.

Model	MSE↓	LPIPS↓	PSNR↑	SSIM↑
KNN-DL	0.716	0.811	1.49	0.107
NeRF ²	0.927	0.958	0.319	0.072
<i>GRaF</i>	0.351	0.688	4.54	0.107

Table 8. Performance on outdoor scene.

Model	MSE↓	LPIPS↓	PSNR↑	SSIM↑
KNN-DL	0.525	0.750	2.82	0.120
NeRF ²	0.851	0.942	0.706	0.119
<i>GRaF</i>	0.208	0.591	6.83	0.148

Table 10. RFID performance after fine-tuning.

Model	MSE↓	LPIPS↓	PSNR↑	SSIM↑
KNN-DL	0.085	0.326	10.73	0.518
NeRF ²	0.107	0.347	10.12	0.492
<i>GRaF</i>	0.049	0.239	15.97	0.618

propagation; the *Outdoor* scene represents a large-scale, open environment with sparse reflectors; and the *RFID* dataset introduces real-world noise, hardware variability, and temporal effects. This evaluation demonstrates the robustness of both models when applied to previously unseen environments beyond their training domain. KNN primarily serves to validate our interpolation theory; thus, we focus on reporting results for KNN-DL, *NeRF*², and *GRaF*.

Analysis. Both *GRaF* and *NeRF*² exhibit degraded synthesis quality when evaluated on scenes that differ significantly from the training layouts, such as environments with unfamiliar furniture or large open spaces. The degradation is more severe for *NeRF*², which collapses into random predictions. In contrast, *GRaF* remains functional, generating spectra that preserve meaningful propagation cues, although its performance also declines. As demonstrated in A.2, the effectiveness of neighboring spectrum weighting is sensitive to transmitter positions. In unfamiliar layouts, these weights become more dynamic and difficult to estimate without explicit scene geometry, leading to reduced synthesis fidelity. KNN-DL also suffers a performance drop under layout shifts, similar to *NeRF*², but still outperforms it by leveraging neighboring spectra. Yet, KNN-DL underperforms compared to *GRaF* due to its reliance on scene-specific learned weights, which generalize poorly.

Despite the drop in synthesis fidelity on unseen layouts, the spatial spectra generated by *GRaF* remain valuable for downstream applications. A key use case is wireless localization, where spatial spectra serve as features to train localization models. For instance, in wireless localization (Section Case Study: Angle of Arrival (AoA) Estimation), they help initialize learning-based localization models more effectively than random initialization.

Fine-Tuning. *GRaF*’s generalization capability improves further with limited fine-tuning. We fine-tune KNN-DL, *GRaF*, and *NeRF*², each pretrained on the conference room layouts, using 20% of the training data from the RFID dataset. While all models benefit from this fine-tuning, *GRaF* achieves the best performance. This advantage stems from its ability to retain propagation priors learned during pretraining, requiring only the refinement of how it integrates neighboring spectra in the new scene. In contrast, *NeRF*² needs to relearn voxel-level attributes from scratch, which limits its adaptability. Similarly, KNN-DL struggles to generalize via fine-tuning under limited data, as it lacks the embedded propagation modeling that enables *GRaF* to transfer effectively across scenes.

E.3. Parameter Study: Number of Neighbors

This section deepens the analysis behind Table 2 (in §5.3 of the main manuscript) by examining how the number of neighbors L influence *GRaF*’s zero-shot spectrum synthesis quality. All evaluations follow the same cross-scene protocol as in §5.3: one model is trained on *ConferenceV1* and tested on *ConferenceV2/V3*, and another is trained on *OfficeV1* and tested on *OfficeV2/V3*, with metrics averaged across all four unseen-scene configurations. All experiments use the 2.412 GHz band (wavelength $\lambda \approx 0.124$ m) and the same settings as in the main manuscript.

For each test transmitter location P , we construct a ranked pool of candidate neighbors by computing Euclidean distances to all training transmitters in the corresponding scene and sorting the points by increasing distance. During model training (as described and conducted in §5.3 of the main manuscript), we randomly sample $L \in [3, 10]$ neighbors for each transmitter to promote robustness to varying neighborhood densities; the Transformer thus learns to fuse an adaptively sized set of neighbors through cross-attention. At test time, we freeze the trained

Table 11. Sensitivity to the number of neighbors L .

L	MSE↓	LPIPS↓	PSNR↑	SSIM↑
2	0.0538	0.274	17.98	0.658
4	0.0417	0.224	20.77	0.699
6	0.0399	0.221	20.88	0.704
8	0.0403	0.219	20.86	0.701
10	0.0396	0.220	20.90	0.709

model and sweep over different values of L in order to analyze how the averaged performance in Table 2 emerges under different neighbor counts.

Number of neighbors L . Table 11 shows the effect of L on spectrum synthesis quality. We fix the radius to $\delta=10\lambda$ and select the first L neighbors from the sorted candidate list for each test location P . Because the model was trained with $L \in [3, 10]$, performance drops noticeably when L falls below this range. With $L=2$, PSNR decreases to 17.98 dB and both MSE and LPIPS degrade substantially. Within the trained interval ($L=4-10$), performance remains stable and exhibits fluctuations of approximately $\pm 0.1-0.2$ dB in PSNR. These small variations reflect scene-dependent geometry. Cluttered regions may benefit modestly from additional neighbors because of richer multipath diversity, while open regions saturate earlier. Overall, the plateau across $L=4-10$ demonstrates the model’s robustness to neighbor count and explains how the averaged performance reported in Table 2 arises across diverse test conditions.

E.4. Computation Overhead

Table 12 summarizes the model size and per-spectrum inference time of *NeRF²* and *GRaF*. As expected, *GRaF* has a larger model footprint (478.6 MB vs. 8.3 MB) and a longer per-spectrum inference time (1.95 s vs. 0.43 s), primarily due to its geometry-aware Transformer and neural ray tracing modules. Unlike *NeRF²*, however, *GRaF* does not require retraining for every new scene. At inference time, neighboring spectra are retrieved directly from the training split of the target scene, incurring no additional data-collection overhead.

Table 12. Comparison of model size and inference time.

	<i>NeRF²</i>	<i>GRaF</i>
Model size (MB)	8.3	478.6
Inference time (s)	0.43	1.95

Although *GRaF* incurs higher per-sample inference overhead, both *NeRF²* and *GRaF* scale linearly with respect to the number of synthesized spectra, making them suitable for large-scale generation tasks. Critically, when considering the *end-to-end* computational cost, including training and inference across multiple scenes, *GRaF* demonstrates higher efficiency. To illustrate this, we compute the total cost required to synthesize 32,625 spectra across the six scenes used in our experiments:

- ***NeRF²***: Each of the six scenes requires scene-specific training (10 hours per scene), totaling 60 hours. Inference adds an additional 3.9 hours (0.43 s per spectrum), leading to a total cost of *63.9 hours*.
- ***GRaF***: A single model is trained once on layout-similar scenes in 15 hours. The inference phase requires 16.2 hours (1.79 s per spectrum), for a total of *31.2 hours*.

Overall, *GRaF* reduces end-to-end computation time by *approximately 51%* compared with *NeRF²*. As the number of layout-similar scenes grows, these gains become even more pronounced because *GRaF* eliminates the need for repetitive scene-specific retraining. Finally, we acknowledge that *GRaF*’s per-spectrum inference latency is higher than that of *NeRF²*. To mitigate this, future work may incorporate *3D Gaussian Splatting*, a technique widely used in optical NeRFs to accelerate rendering by replacing dense voxel sampling with adaptive, compact Gaussian primitives.

E.5. Impact of RF Frequency Bands

GRaF performs well when trained and tested within the same RF frequency band, but it does not generalize across different bands. This behavior is expected because wireless propagation is fundamentally *frequency-dependent*: reflection strength, diffraction angles, penetration depth, and scattering characteristics all vary with wavelength. As a result, the spatial spectrum at one frequency band cannot be reliably inferred from measurements at another. In practice, wireless communication systems are intentionally engineered to operate within *specific, standardized frequency bands*. Each band corresponds to distinct antenna designs, hardware front-ends, propagation characteristics, and communication protocols. Examples include:

- **1.8 GHz (4G LTE)**: Optimized for wide-area coverage with relatively strong penetration. Devices use antenna and RF chains tailored to mobile broadband protocols such as OFDMA and SC-FDMA, enabling stable performance across large outdoor regions.
- **2.4 GHz (WiFi / WLAN)**: Designed primarily for indoor deployments. Propagation is more sensitive to multipath and clutter from walls and furniture, and IEEE 802.11 protocols focus on robust medium access and interference mitigation in dense indoor environments.
- **3.0 GHz (5G NR)**: Used in mid-band 5G with advanced hardware such as beamforming arrays and massive MIMO. Propagation exhibits reduced penetration and stronger directionality, and the 5G NR standard leverages these properties for high-capacity, low-latency communication.

These bands differ not only in propagation physics but also in system-level design: antenna geometries, transceiver circuitry, channel coding, and deployment conditions all diverge across frequencies. Consequently, a model trained at one frequency band cannot meaningfully generalize to another because the underlying spatial spectrum statistics shift with wavelength. For this reason, *GRaF* is intentionally designed for *per-band* spatial spectrum synthesis, which mirrors how real-world wireless systems operate. In practice, building separate models for each frequency band is both realistic and necessary for producing physically accurate RF spectrum predictions.

F. Discussion

F.1. Rationale for Using Neighboring Spectra

While *GRaF* conditions on L sparse nearest-neighbor spectra at inference, this does not contradict our generalization claim. *GRaF* generalizes in the standard sense established by generalizable NeRFs: the model is trained *once* on a set of scenes and then directly applied to entirely new scenes *without any per-scene retraining or optimization*. The use of sparse neighbors is not a limitation, but a principled design choice mandated by our RF Spatial Spectrum Interpolation Theorem (Theorem 1), which proves that the spectrum at a target location can be approximated using spectra from geographically proximate transmitters with a *quadratically bounded* error. This behavior is inherent to RF propagation physics, where spatial smoothness and local continuity are well established (*e.g.*, path loss, diffraction, and multipath exhibit coherent local variations).

From a practical standpoint, obtaining L sparse neighbors is lightweight and realistic in real RF deployments. Modern WiFi/6G environments already contain multiple active transmitters, and sparse measurements can be obtained via quick walk-by scans, automated robot traversals, or even existing network infrastructure with negligible overhead. In contrast, *NeRF²*/*NeWRF* require *dense* per-scene measurements (thousands of samples) and full per-scene model training, making them significantly more expensive to deploy. *GRaF* requires only a handful of conditioning samples and *no per-scene optimization*, reducing both measurement and computational cost by orders of magnitude.

Empirically, our cross-scene, cross-layout, and cross-environment experiments (Tables 2–3 and Supplementary Materials §E) demonstrate that *GRaF* consistently outperforms KNN, KNN-DL, and *NeRF²* on unseen scenes despite using only sparse neighbors. These results confirm that conditioning on sparse local spectra *enables* practical and scalable generalization rather than limiting it. *GRaF* achieves strong generalization because it leverages (i) a scene-independent latent RF radiance field learned from diverse training scenes and (ii) physically grounded sparse conditioning aligned with RF interpolation theory, rather than relying on scene-specific overfitting or dense retraining.

F.2. Limitations and Possible Solutions

Despite the promising performance of our method, several limitations remain.

First, although *GRaF* generalizes well to scenes with moderately similar structures, its performance degrades when the new scene differs substantially from the training layouts. In such cases, a small amount of additional spectrum data may be required for scene-specific fine-tuning. This motivates future work on more expressive latent RF radiance fields that can better disentangle universal propagation behaviors from scene-dependent geometry.

Second, our current framework focuses on spatial generalization and does not explicitly address temporal dynamics. Real-world RF environments exhibit temporal variations caused by moving objects, human activity, or environmental changes. A promising direction is to extend *GRaF* with a deformable or time-aware latent RF radiance field that can capture temporal evolution, enabling continuous adaptation without full retraining.

Finally, *GRaF* assumes access to sparse neighboring spectra at inference, which is lightweight but still requires minimal on-site measurements. Future research may explore hybrid approaches that combine *GRaF* with predictive physics-based models or self-supervised priors, further reducing measurement requirements and enabling fully zero-shot deployment in unseen environments.